Received: 2 November 2020 | Revised: 28 March 2021 | Accepted: 2 May 2021

DOI: 10.1111/nan.12734

Neuropathology and Applied Neurobiology WILEY

ORIGINAL ARTICLE

Prodromal sensory neuropathy in *Pink1*$^{-/-}$*SNCA*^{A53T} double mutant Parkinson mice

Lucie Valek[1] | Bao Tran[1] | Annett Wilken-Schmitz[1] | Sandra Trautmann[1] | Juliana Heidler[2] | Tobias Schmid[3] | Bernhard Brüne[3,5] | Dominique Thomas[1] | Thomas Deller[4] | Gerd Geisslinger[1,5,6] | Georg Auburger[7] | Irmgard Tegeder[1]

[1]Institute for Clinical Pharmacology, Faculty of Medicine, Goethe-University of Frankfurt, Frankfurt, Germany

[2]Functional Proteomics Group, Faculty of Medicine, Goethe-University, Frankfurt, Germany

[3]Institute of Biochemistry I, Faculty of Medicine, Goethe-University of Frankfurt, Frankfurt, Germany

[4]Institute of Clinical Neuroanatomy, Faculty of Medicine, Goethe-University of Frankfurt, Frankfurt, Germany

[5]Fraunhofer Institute for Translational Medicine and Pharmacology ITMP, Frankfurt, Germany

[6]Fraunhofer Cluster of Excellence for Immune Mediated Diseases (CIMD), Frankfurt, Germany

[7]Experimental Neurology, Faculty of Medicine, Goethe-University, Frankfurt, Germany

Correspondence
Irmgard Tegeder, Institute of Clinical Pharmacology, Goethe-University, Medical Faculty, Frankfurt, Germany.
Email: tegeder@em.uni-frankfurt.de

Funding information
The study was supported by the Deutsche Forschungsgemeinschaft CRC1039 (A03 to IT; Z1 to GG), CRC1080 (C02 to IT, B03 to TD), SFB815 (A12 to IT; A08 to BB; Z1 to JH) and by the Fraunhofer Cluster of Excellence for immune mediated diseases (CIMD, to GG).

Abstract

Aims: Parkinson's disease (PD) is frequently associated with a prodromal sensory neuropathy manifesting with sensory loss and chronic pain. We have recently shown that PD-associated sensory neuropathy in patients is associated with high levels of glucosylceramides. Here, we assessed the underlying pathology and mechanisms in *Pink1*$^{-/-}$*SNCA*^{A53T} double mutant mice.

Methods: We studied nociceptive and olfactory behaviour and the neuropathology of dorsal root ganglia (DRGs), including ultrastructure, mitochondrial respiration, transcriptomes, outgrowth and calcium currents of primary neurons, and tissue ceramides and sphingolipids before the onset of a PD-like disease that spontaneously develops in *Pink1*$^{-/-}$*SNCA*^{A53T} double mutant mice beyond 15 months of age.

Results: Similar to PD patients, *Pink1*$^{-/-}$*SNCA*^{A53T} mice developed a progressive prodromal sensory neuropathy with a loss of thermal sensitivity starting as early as 4 months of age. In analogy to human plasma, lipid analyses revealed an accumulation of glucosylceramides (GlcCer) in the DRGs and sciatic nerves, which was associated with pathological mitochondria, impairment of mitochondrial respiration, and deregulation of transient receptor potential channels (TRPV and TRPA) at mRNA, protein and functional levels in DRGs. Direct exposure of DRG neurons to GlcCer caused transient hyperexcitability, followed by a premature decline of the viability of sensory neurons cultures upon repeated GlcCer application.

Conclusions: The results suggest that pathological GlcCer contribute to prodromal sensory disease in PD mice via mitochondrial damage and calcium channel hyperexcitability. GlcCer-associated sensory neuron pathology might be amenable to GlcCer lowering therapeutic strategies.

KEYWORDS
Parkinson's disease, pain, sensory loss, alpha-synuclein, PTEN inducible kinase 1, glucosylceramides, innate immunity, mitochondrial respiration

INTRODUCTION

Parkinson's disease (PD) is a complex neurodegenerative disease that primarily affects motor systems of the basal ganglia and manifests with muscle rigidity, tremor, slowness of movement and difficulty walking.[1] PD also involves multiple extranigral brain regions and the peripheral nervous system [2] leading to non-motor symptoms, particularly olfactory dysfunction, rapid eye movement (REM) sleep disorder, dysautonomia, restless leg disorder [3-7] and chronic pain that presents as musculoskeletal, neuropathic, visceral and dystonic pain and is highly prevalent in PD patients.[8-13]

PD-associated pain is frequently associated with small or mixed fibre sensory neuropathies involving somatosensory and autonomic nerves.[14-18] Patients often complain about constipation, visceral discomfort and pain, gut and bladder dysfunction and deregulation of exocrine glands. A loss of somatosensation may remain unnoticed, unless it is associated with burning pain in the hands and feet.[19] The progressive loss of sensory function parallels the progression of the disease, but may precede motor symptoms for more than 10 years,[19,20] suggesting that sensory neurons are particularly vulnerable and likely represent a source of the propagation of prion-like alpha-synuclein.[21-23]

The predominant morphological features of PD are intraneuronal alpha-synuclein-rich deposits, the major components of Lewy bodies,[2,24,25] but the pathophysiology is only partly understood. Mitochondrial damage and dysfunction of protein degradation via the proteasome and via autophagolysosomes contribute to the progressive loss of dopaminergic and other neurons. Defective mitophagy can lead to leakage of mitochondrial DNA to the cytosol that triggers innate immune system responses.[26]

It has been recognized in recent years that metabolic deregulation of bioactive lipids including ceramides and their metabolites increases the toxicity of alpha-synuclein.[27-29] Patients who are heterozygous carriers of glucocerebrosidase (*GBA1*) mutations tend to develop a rapidly progressive disease,[30] and such mutations propagate alpha-synuclein deposition in PD model organisms.[31-34] *GBA1* mutations constitute the highest independent genetic risk factor for sporadic PD.[35]

GBA1 is a lysosomal enzyme that catalyses the degradation of ceramides to glucosylceramides (GlcCer) and the subsequent generation of lactosylceramides (LacCer) and gangliosides. Low *GBA1* activity and accumulation of GlcCer even occur in PD patients without known mutations of *GBA1* [8,36,37] and point at a link between PD and Gaucher disease, a lysosomal storage disorder that is caused by homozygous loss-of-function mutations of *GBA1*.[38]

We have recently shown in patients with sporadic PD that high concentrations of plasma GlcCer are associated with pain ratings and with sensory loss as assessed by quantitative sensory testing,[8] suggesting that GlcCer may contribute to the progression of the disease from peripheral sensory neurons to the brain and to clinical PD-associated pain.[8] GlcCer are components of membrane barriers and maintain organelle curvature, but overloading interferes with the lysosomal membrane charge and leads to leakage.[39] It also accumulates in mitochondrial membranes.[40] Hence, GlcCer constitutes a link between lysosomal and mitochondrial pathology in PD.

There are no remedies that specifically alleviate PD-associated pain or prevent sensory loss,[41,42] in part owing to limited knowledge of PD-associated somatosensory pathology in model organisms. Motor function and the morphological characteristics of PD have been studied in several rodent, primate and fly disease models, but sensory function and the underlying pathological features of sensory neurons have been rarely addressed,[43] and the few studies of non-motor manifestations such as olfaction, anxiety-like behaviour and gastrointestinal function are fragmented and, in part, inconclusive.

In the present study, we used a previously described *Pink1*$^{-/-}$*SNCA*^{A53T} double mutant mouse model of PD [44] to study pre-motor sensory phenomena, and biological and morphological correlates to reveal the underlying pathophysiological mechanisms and the progressive nature of the sensory loss, with a focus on the sphingolipid pathology. *Pink1*$^{-/-}$*SNCA*^{A53T} mice carry a loss of function knock-in mutation of *PTEN* induced kinase (*Pink1*), plus the human A53T mutation of alpha synuclein (*SNCA*-A53T). These *Pink1*$^{-/-}$*SNCA*^{A53T} mice develop spontaneous motor symptoms at advanced ages, with a progressive incidence above 15 months of age.

We show that sensory deficits occur early and are associated with accumulation of GlcCer in somatosensory neurons of the dorsal root ganglia, mitochondrial ultrastructural pathology in specific neurons and deregulation of transient receptor potential channels that can explain the loss of sensory functions. The data strengthen the pathological role of glucosylceramides and should encourage glycosphingolipid-directed therapeutic approaches.

METHODS

Mouse strains

Homozygous *Pink1*$^{-/-}$ plus *SNCA* A53T double mutant mice were generated by crossing *Pink1*$^{-/-}$ mice (background: 129/SvEv) with *A53T-SNCA*-overexpressing PrPmtA mice (background: FVB/N) and then, interbreeding the littermates. They contain 129/SvEv and FVB/N genetic backgrounds approximately in a 50:50 distribution. Wild-type (WT) control mice are hybrids from a crossbreeding of 129/SvEv and FVB/N mice, which were descended from littermates of the respective single mutant animals. The double mutant mice are referred to as *Pink1*$^{-/-}$*SNCA*^{A53T} or in short, *Pink1SNCA*.

Mice had free access to food and water, and they were maintained in climate-controlled rooms with a 12 h light-dark cycle. Behavioural experiments were performed between 10 am and 3 pm. The experiments were approved by the local Ethics Committee for animal research, adhered to the guidelines for pain research in conscious animals of the International Association for the Study of PAIN (IASP) and those of the Society of Laboratory Animals (GV-SOLAS)

and were in line with the European and German regulations for animal research.

Analysis of nociception and somatosensory function

Nociceptive tests were performed at 2, 4, 10 and 12 months of age with 8 mice per group. Mice were habituated to the test room and the test chambers for three consecutive days before the baseline measurements.

The latency of paw withdrawal on point mechanical stimulation was assessed using a Dynamic Plantar Aesthesiometer (Ugo Basile). The steel rod was pushed against the plantar paw with ascending force (0–5 g, over 10 s, 0.2 g/s) and then maintained at 5 g until the paw was withdrawn. The paw withdrawal latency was the mean of three consecutive trials with at least 30 s intervals.

The sensitivity to painful heat stimuli was assessed by recording the paw withdrawal latency with a Hot Plate (52°C or 30–55°C surface) or with the Hargreaves test (IITC Life Science). In the latter, an infrared lamp was placed with a mirror system underneath the respective hind paw. By pressing the start button the lamp starts to emit a heat-beam until the paw is withdrawn, which stops the lamp. The mean of three replicate tests was used for statistical analysis.

The Orofacial Pain Assessment Device (OPAD, Stoelting) allows for evaluation of facial thermal nociception by using a reward-conflict paradigm. The OPAD cage consists of a plexiglass chamber with metal grid floor and an adjustable slit giving access to the nipple of the reward bottle. The slit is flanked with PC-controlled thermal peltier elements. To receive the reward (diluted milk in water), the mouse has to touch the thermodes with its cheeks. Mice were fasted overnight to increase their appetite. Mice were trained three times a week for 2 weeks at innocuous temperatures (36.5–38°C) to get a stable baseline of at least 600 licks in 18 min. During test periods, temperature circles starting from neutral (37°C, 3 min) to aversive cold (15°C, 10°C each 3 min) or aversive heat (45°C, 54°C each 3 min) were applied using a ramping protocol. Circles were repeated up to 20 min. The ANY-maze software (Version 4.99, Stoelting) registered licks and contacts with the thermodes. The average and total numbers of lickings and contacts at the defined temperatures were used for analysis. Ramping times were excluded.

Thermal gradient ring

A thermal gradient ring (Ugo Basile) was used to assess the temperature preferences and exploration of the ring platform.[45] The TGR provides a circular running track for the mouse to move freely.

The dimensions of inner and outer ring diameters are 45 and 57 cm. Inner walls of plexiglass and outer walls of aluminium, both of 12 cm height, build a 6 cm wide circular running arena. The aluminium surface provides a temperature gradient, controlled with two peltier elements. Infrared cameras constantly measure the temperature. The arena is divided into mirror semicircles of each 8–12 zones. During measurements, the running track is illuminated and the mouse behaviour is videotaped with a regular CCD camera, mounted above the mid-point of the ring. The time spent in zones and temperature preferences are analysed automatically with the TGR ANY-Maze video tracking software (Stoelting).

Olfactory and motor functions

Behavioural studies of olfactory sensitivity and discrimination, motor functions and Phenomaster analyses of drinking, feeding and voluntary wheel running are explained in the Data S1.

Culture and staining of primary DRG neurons

Primary adult dissociated DRG neuron-enriched cultures were prepared by dissecting mouse dorsal root ganglia (DRGs) into 1x PBS (Phosphate Buffered Saline, Gibco), followed by digestion with 5 mg/ml collagenase A and 1 mg/ml dispase II (Roche Diagnostics). Triturated cells were centrifuged through a 15% BSA (bovine serum albumin) solution and plated on poly-L-lysine and laminin coated cover slips in Neurobasal medium (Gibco) containing 2% (vol/vol) B27 supplement (Gibco), 50 µg/ml Pen-Strep, 100 ng/ml NGF and 200 mM L-glutamine. After incubation for 2 h, 2 ml Neurobasal medium was added, and neurons were cultured for up to 48 h depending on the experimental requirements. Cells were kept at 37°C, 5% CO_2, 95% humidity. Primary DRG neurons were used for calcium imaging and immunohistochemical staining.

To assess the effects of GlcCer24:1 (Avanti Polar Lipids, #860549P) on outgrowth, morphology and excitability neurons were cultured in the presence of 1–10 µM GlcCer24:1 or vehicle, starting at plating of the neurons. The vehicle was a 2:1 mixture of chloroform and methanol, the final dilution of the vehicle was 1:10 000 or 1:1000, respectively. For assessment of culture longevity, tiled images of live cultures were captured daily to assess the whole coverslip. Culture density was assessed by analysing the percentage area covered with neurons and dendrites using FIJI ImageJ. After background subtraction, thresholds were set using Li's algorithm, and binarized images were analysed using the particle counter. For immunofluorescence studies, cultures were washed and subsequently fixed with 4% paraformaldehyde in 1x phosphate buffered saline (PBS) at 24 or 48 h. Immunostaining was performed for neuronal marker (NF200, TUJ1), alpha synuclein, the growth cone marker, phalloidin-Alexa594 and nuclear DAPI to assess outgrowth, dendritic trees, morphology and viability. Arborization was assessed using Scholl-analysis implemented in ImageJ.

Calcium imaging

Calcium influx in sensory neurons upon stimulation with capsaicin is a biological correlate of nociceptive sensitivity.[46-48] Capsaicin is a

major constituent of chilli peppers and causes burning pain *in vivo* via activation of transient receptor potential channels, TRPV1. To assess the effects of GlcCer24:1, cultures were treated for 24 or 48 h with 1 μM GlcCer24:1.

Calcium fluxes were measured fluorometrically as the ratio of the absorbances at 340 and 380 nm (F 340/380) in cultured adult DRG neurons. Calcium-imaging experiments were performed with a Leica calcium-imaging setup. Images were captured every two seconds. Cells were loaded with 5 μM of the Ca^{2+}-sensitive fluorescent dye Fura-2-AM-ester, incubated for 40 min at 37°C and washed three times with ringer solution. Coverslips were then transferred to a perfusion chamber with a flow rate of 1–2 ml/min at room temperature. Baseline ratios were recorded for 100–180 s, before application of either 0.01% formalin to activate TRPA1 or 50 nM capsaicin (Sigma) to activate TRPV1 ion channels for 100 s or 26 s, respectively. After wash-out with Ringer solution, cells were perfused with 100 mM KCl (high K+) to assess depolarization-evoked calcium currents and the viability of the neurons. Data are presented as changes in fluorescence ratios (F340/380) normalized to baseline ratios. The analysis encompassed 300–350 neurons per condition of 10–12 independent DRG cultures of each three mice per group per stimulus, which were 18 months old. The maximum, the time of maximum and area of the fold increase versus time curve was calculated by integration (Origin Pro 2020 software) with the baseline fixed at Y = 1. The time courses and areas were used for statistical comparison. The GlcCer experiment encompassed five independent parts each with 6/6 DRG neuron cultures and in total, 591 and 594 neurons for control and GlcCer, respectively.

RNA analyses

Quantitative RT-PCR (qRT-PCR) were done according to standard procedures (Data S1) using Primers described in Table S1a.

RNA sequencing and data analysis is described in Data S1 and was essentially as described in Ref. [49].

Immunohistochemistry

Mice were terminally anaesthetized with isoflurane and transcardially perfused with cold 0.9% NaCl followed by 2% paraformaldehyde (PFA) for fixation. Tissues were excised, post-fixed in 2% PFA for 2 h, cryoprotected overnight in 20% sucrose at 4°C, embedded in small tissue moulds in cryo-medium and cut on a cryotome (10 μm for DRGs and ScN, 12 μm for SC). Slides were air-dried and stored at −80°C. After thawing, slides were immersed and permeabilized in 1xPBS with 0.1% Triton-X-100 (PBST), then blocked with 3% BSA/PBST, subsequently incubated overnight with the first primary antibodies in 1% BSA/PBST at 4°C. After washing three times with PBS, slides were incubated with the secondary antibodies for 2 h at room temperature, followed by 10 min incubation with DAPI and embedding in Aqua-Poly/Mount. The general settings were optimized for the respective antibodies and tissues. Primary antibodies are listed in Table S1b. Secondary antibodies were labelled with fluorochromes (Invitrogen, Sigma, Life Technologies). Slides were analysed on an inverted fluorescence microscope (BZ-9000, KEYENCE, Germany and Axio Imager Z1, Zeiss).

For analysis of neurite outgrowth and morphology, primary neuron cultures were washed in PBS, fixed in 4% PFA and immunostained with primary antibodies (Table S1). Tiled images were captured on an inverted Axio Imager Z1 fluorescence microscope (Zeiss). For quantification, RGB images were converted to binary images using threshold setting implemented in ImageJ, and the particle counter was used to assess the area covered with neuronal immunoreactive structures.

Transmission electron microscopy

Mice were terminally anaesthetized with carbon dioxide and perfused transcardially with cold 0.9% sodium chloride (NaCl) followed by perfusion with the fixation solution containing 4% PFA and 4% glutaraldehyde in 0.1 M cacodylate buffer, pH 7.4. DRGs were excised and post-fixed in the fixation solution for 90 min. After washing three times with 0.1 M cacodylate buffer, the tissue was osmicated (1% OsO_4 in 0.1 M cacodylate buffer) for 60 min, washed three times with 0.1 M cacodylate buffer and dehydrated in ethanol, 1% uranyl acetate and propylene oxide. The tissue was then incubated in Durcupan resin (Fluka, Durcupan ACM-Kit) overnight and embedded in fresh Durcupan resin at 56°C for 48 h. Ultrathin sections (54 nm) were cut with a diamond blade, collected on single slot Formvar-coated copper grids and contrasted with lead citrate. Sections were analysed using a Zeiss electron microscope (Zeiss EM900) and imaged with a slow-scan CCD-Camera. The area, width and brightness of white mitochondria was measured with the respective tools in FIJI ImageJ.

Oxygraph analysis of mitochondrial OXPHOS activity

Brain sections (prefrontal cortex, hippocampus), DRGs, and trigeminal nerve and ganglia were immediately transferred into ice-cold Respiration medium MiR06Cr containing 280 U/ml catalase. Tissue was homogenized using a motor-driven tightly fitting glass/Teflon Potter-Elvehjem homogenizer. Mitochondrial respiration was measured using high-resolution respirometry (Oxygraph-2k, Oroboros Instruments) with DatLab software 6.1.0.7 (Oroboros Instruments). A "substrate-uncoupler-inhibitor titration" protocol was used essentially as described in Ref. [46]. LEAK-respiration was induced by the addition of complex I – linked substrates pyruvate (5 mM), malate (0.5 mM) and glutamate (10 mM). Complex I – linked respiration was measured after adding ADP (2.5 mM) in a saturating concentration. To measure complex II-linked respiration, rotenone (0.5 μM) was added to block complex I followed by the addition of succinate (10 mM). Maximum uncoupled respiration (ETS, electron transfer system capacity) was

measured after stepwise titration of FCCP (carbonyl cyanide-p-trifluo rmethoxyphenylhydrazone). Residual oxygen consumption (ROX) was determined after sequential inhibition of complex III with Antimycin A and complex IV with azide. Absolute respiration rates were corrected for ROX and normalized for the protein content. Citrate synthase activity was measured to confirm comparable numbers of mitochondria.

Lipid analyses

Lipid analyses were done as described previously [50] and are briefly explained in Data S1.

RNA sequencing and data analysis is described in Data S1 and was essentially as described in Ref. [50].

Statistics

Group data are presented as mean ± SD or mean ± SEM, the latter for behavioural time course data, specified in the respective figure legends. Data were analysed with SPSS 24 and Graphpad Prism 8.0 and Origin Pro 2020. Data were mostly normally distributed, or log-normally distributed. For testing the null-hypothesis that groups were identical, the means of two groups were compared with 2-sided, unpaired Student's *t* tests. The Mann–Whitney *U* test was used as a non-parametric alternative in case of violations of *t* test requirements. Time course data or multifactorial data were submitted to two-way analysis of variance (ANOVA) using e.g., the factors 'time' and 'genotype'. For respirometry, the within subject factor "stimulus" and between subject factor "group" were used. In case of significant differences, groups were mutually compared at individual time points using post hoc *t* tests according to Dunnett or according to Šidák or Holm-Šidák. In case of violations of sphericity, degrees of freedom were adjusted according to Huynh Feldt. Asterisks in figures show multiplicity-adjusted *p*-values. The areas under the curve of calcium imaging data that were Log2-transformed the areas were calculated by integration. Data distribution was obtained by Kernel density estimation (Origin Pro).

Principal component analysis was used to define the lipid species, which accounted most for the variance between genotypes. Further multivariate analyses included canonical discriminant analysis to assess the predictability of group membership and separation of genotypes and tissues.

RESULTS

Loss of thermal nociception in middle-aged *Pink1*$^{-/-}$*SNCA*^{A53T} mice

Pink1$^{-/-}$*SNCA*^{A53T} mice had normal paw withdrawal latencies upon mechanical stimulation but showed a strong loss of thermal heat sensitivity in Hargreaves and Hotplate tests (Figure 1A), and they preferred cooler temperatures in a Thermal Gradient Ring (TGR) test, in which mice can freely choose their temperature of well-being (Figure 1B). The TGR behaviour suggested paradoxical heat sensation and loss of cold sensation, which was confirmed for trigeminal hot/cold stimulation in the Orofacial Pain Assessment Device (OPAD), in which mice have to touch heated or cooled metal bars to get access to a rewarding milk bottle. *Pink1*$^{-/-}$*SNCA*^{A53T} showed a preference for unpleasant cold temperatures when compared to WT mice (Figure 1C).

Nociceptive tests were repeated in younger mice to assess the onset of thermal sensory loss. There were no differences at 2 months of age between mutant and WT mice. The first significant protraction of paw withdrawal upon heat stimulation occurred at 4 months of age (Figure 1D), hence at least 11 months before the earliest occurrence of spontaneous motor deficits.

There was no sensory loss in single mutant mice at 9–10 months of age but rather nociceptive hypersensitivity in *Pink1*$^{-/-}$ mice (Figure 1E), possibly suggesting that polyneuropathy in PD mice progresses from hyperexcitability if only *Pink1* is missing towards sensory loss in the additional presence of mutant *SNCA*.

No impairment of basic health or motor functions in middle-aged *Pink1*$^{-/-}$*SNCA*^{A53T} mice

General health and motor function are prerequisites for sensory tests, which rely on paw withdrawal or locomotion, and were therefore assessed in parallel (Figure S1A–G). In adult life, up to middle age (9–10 months of age), *Pink1*$^{-/-}$*SNCA*^{A53T} mice had normal body weights (Figure S1A), but higher feeding and drinking than wild-type mice in enriched environmental settings of Phenomaster cages (Figure S1A), whereas drinking and feeding were alike in metabolic cages (not shown). High locomotion in social olfactory tests (Figure S1G) also suggested some overactivity in enriched environments.

Middle aged *Pink1*$^{-/-}$*SNCA*^{A53T} mice behaved normally in most motor function tests including grip strength, voluntary wheel running and distances travelled in mazes (Figure S1A,G), but half of the *Pink1*$^{-/-}$*SNCA*^{A53T} mice did not reach the target running time of 5 min in the accelerating Rotarod test (Figure S1A). Younger mice, at 20 weeks of age, also needed more trials to reach the 5 min running goal (Figure S1B), whereas all wild-type controls succeed on the first or second training run. Hence, *Pink1*$^{-/-}$*SNCA*^{A53T} mice had a mild impairment of motor coordination. Single mutant mice showed normal Rotarod running. The cohort of *Pink1*$^{-/-}$ mice had lower body weights than their wild-type controls, but without an effect on other markers of general health (Figure S1C).

Loss of nutritive olfaction in middle-aged *Pink1*$^{-/-}$*SNCA*^{A53T} mice

PD-associated polyneuropathy often co-manifests with loss of olfaction. We therefore also assessed nutritive and

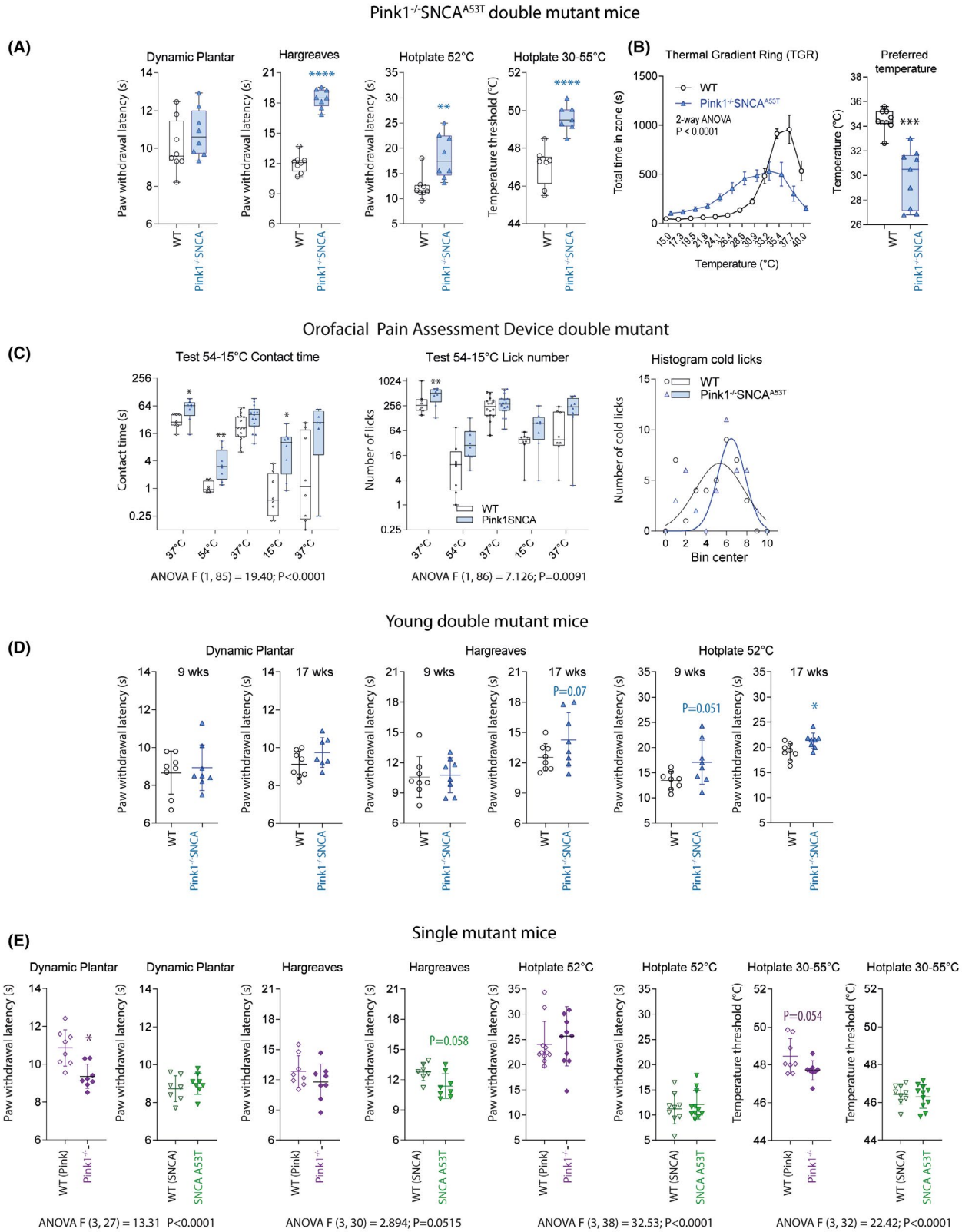

social olfactory behaviour (Figure S1D–G). In the Novel Odour Recognition and memory test, *Pink1*$^{-/-}$*SNCA*^{A53T} mice were less interested in the pleasant odours, vanilla or rose, as compared to wild-type control mice (Figure S1D), but they were able to discriminate between vanilla (preferred odour) and rose, like the controls (Figure S1D). They did not reach out to the sweet pellets presented on the steps of a staircase test (Figure S1F), which is supposed to measure motor function but also relies on the awareness of the sweet reward. Mice were 15 months old for the staircase test.

FIGURE 1 Somatosensory behaviour of double mutant *Pink1*$^{-/-}$*SNCA*^{A53T} mice and of single mutant mice. (A) Nociceptive paw withdrawal latencies on mechanical (dynamic plantar test) and heat stimulation (Hargreaves and Hot Plate) in middle aged *Pink1*$^{-/-}$*SNCA*^{A53T} double mutant mice at 9 months of age. Hot plates had constant 52°C or dynamically increased temperature. (B) Preference temperatures on a Thermal Gradient Ring (TGR) with a temperature gradient of 15–40°C in middle aged *Pink1*$^{-/-}$*SNCA*^{A53T} double mutant mice at 10 months of age. (C) Trigeminal sensory functions assessed in an Orofacial Pain Assessment Device (OPAD) in 12 months old *Pink1*$^{-/-}$*SNCA*^{A53T} double mutant mice. Box/Scatter plots show contact times with metal bars and lickings at the respective temperatures. For the histogram, all licks at the cold temperatures (7, 10 and 15°C) were pooled and fitted to a Gauss distribution. (D) Nociceptive paw withdrawal latencies on mechanical (dynamic plantar test) and heat stimulation (Hargreaves and Hot Plate) in young *Pink1*$^{-/-}$*SNCA*^{A53T} double mutant mice at 9 and 17 weeks of age. (E) Nociceptive paw withdrawal latencies on mechanical (dynamic plantar test) and heat stimulation (Hargreaves and Hot Plate) in 9–10 months old *Pink1*$^{-/-}$ knockout and *Pink1* wild-type mice, and in a single mutant *SNCA*-A53T and *SNCA* wild-type mice. Please note that single and double mutant lines each have its wild-type control line to match the respective genetic backgrounds. *Pink1* has a 129/SvEv background and *SNCA* a FVB/N background. WT controls of *Pink1*$^{-/-}$*SNCA*^{A53T} double mutant mice have a mixed background identical to the double mutant mice. Age and gender matched pairs were used in all experiments. The scatter show results of individual mice. Sample sizes were 8–9 mice for all experiments. The box shows the interquartile range, the whiskers show minimum to maximum. Groups were compared with unpaired, two-sided Student's *t* tests or ANOVA according to the number of groups and data structure. OPAD data were compared with ANOVA for repeated measurements followed by post hoc comparison with correction of alpha according to Šidák. In E, data of single mutant mice were compared with two-way ANOVA followed by post hoc Šidák. Asterisks show adjusted *p* values with significant difference at $^{*}p < 0.05$, $^{**}p < 0.001$, $^{***}p < 0.0001$

In the social odour recognition test (urine mixtures), *Pink1*$^{-/-}$*SNCA*^{A53T} responded equally to the social odour and were more attracted to the novel odour relative to the familiar odour (Figure S1E). They were hyperactive in this social setting, as reflected by longer travel distances in this test (Figure S1G). Sensation and processing of pleasant odours in mice requires dopaminergic neurons of the olfactory bulb, which are a primary site of PD pathology, whereas social odours depend on neurons of the vomeronasal organs and accessory olfactory bulb,[51] which are less affected in PD mice. Their behaviour, therefore, agrees with a preferential DA-neuron loss in the olfactory bulb.

Accumulation of glucosylceramides in DRGs and loss of sphingolipids in the sciatic nerve

We have previously shown in PD patients, that sensory loss and pain owing to PD-associated polyneuropathy were linearly associated with high plasma GlcCer.[8] Hence, we hypothesized that PD associated polyneuropathy is caused, at least in part, by GlcCer accumulation in sensory neurons. To address this hypothesis, sphingolipids of different classes were analysed in DRGs, sciatic nerve (ScN), spinal cord (SC) and plasma from 12 months old *Pink1*$^{-/-}$*SNCA*^{A53T} and wild-type control mice ($n = 8$ per group). The analysis encompassed dehydro-ceramides, ceramides, glucosyl- and lactosylceramides, as well as sphinganine, sphingosine and the respective phospho-SPH. Levels in plasma (not shown) and spinal cord (Figure S2) did not differ between groups, but there were substantial differences in DRGs and ScN (Figure 2 overview, 3 candidates per site).

Discriminant Principal Component (PC) Analysis using the lipids in DRGs and ScN as inputs revealed that GlcCer16:0 (increased), SPHs (decreased) and LacCer24:1 (decreased) accounted for most of the variance between groups (Figure 2A). Site specific concentrations of candidate lipids and the ANOVA statistics are shown in Figure 3.

Based on PC1 and PC2, groups were clearly separated (Figure 2A), and group membership was predictable using three key lipids, GlcCer16:0, LacCer24:1 and S1P18.0 (3D plot, Figure 2B). Pairs of lipids were further compared in a scatter matrix (Figure S2A) and revealed a clear group separation based on GlcCer16:0 versus either sphinganine (SPH18:0) or sphinganine-1-phosphate (S1P18:0). Polar plots of normalized mean lipids reveal the tissue specific patterns of sphingolipid alterations (Figure 2C; Figure S2C for spinal cord), which are also demonstrated by scatter plots of canonical discriminant scores (Figure S2B). The accumulation of ceramides also manifested as an increase of ceramide immunofluorescence in cultured DRG neurons obtained from 12 months old mice (Figure 2D).

In the DRGs, the accumulation of ceramides predominated whereas loss of sphingosines and sphinganines predominated in the sciatic nerve (Figure 3). Hence, GlcCer accumulates in somata, likely with a gain of toxic function, and downstream SPH metabolites are missing in axons, likely resulting is a loss of function. It is of note that the alteration of the signalling lipids was not associated with a disruption of the citrate cycle, which requires metabolic lipids, as revealed by normal citrate synthase levels in the DRGs (Figure S2D). Normal citrate synthase levels suggested normal mitochondrial numbers. However, mitochondrial damage is a predominant feature of PD, and GlcCer accumulation likely disrupts organelle membranes. Therefore, we studied mitochondrial morphology and respiratory function to assess a link between GlcCer and mitochondrial pathology.

Mitochondrial pathology in distinct DRG neurons with reduced mitochondrial respiration

Based on the lipid patterns, we expected that GlcCer overload would be associated with pathological alteration of organelle morphology and function.[39,52] We analysed the ultrastructural morphology of DRGs of 15–17 months old mice to address this hypothesis (Figure 4).

There were no overt differences in terms of cellularity, neuron number or shape, myelin sheaths or vascular cells between genotypes (Figure 4). DRG neurons of both genotypes showed a high

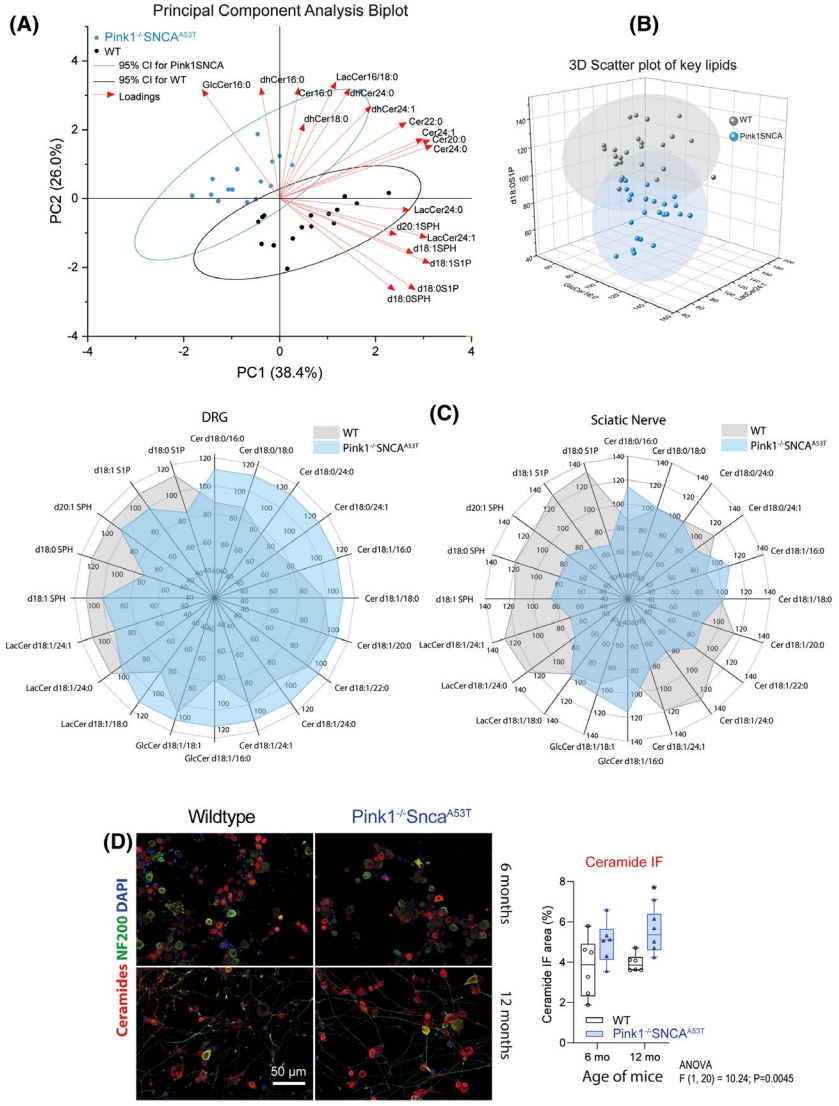

FIGURE 2 Ceramides and sphingolipids in DRGs, sciatic nerve and spinal cord. (A) Principal component analysis (PCA) biplot of lipids in DRGs and sciatic nerve (ScN) of eight mice per genotype and site (age 12 months). Percentages were used as PCA input because total lipid concentrations differ by several orders of magnitude. The respective lipid mean of all samples was set to 100%. The loadings are presented as arrows. The dots are individual mice, and each mouse is represented twice for DRG and ScN. The ellipses show the 95% CI. (B) 3D scatter plot of three lipid species of three classes, which differed most between genotypes: GlcCer 16:0, sphinganine (d18:0 SPH) and LacCer 24:1. The data are percentages of each lipid (relative to the mean set to 100%) for each tissue. Hence, each mouse is represented three-times for DRG, ScN and SC. The ellipsoids show the 95% CI. (C) Polar plots of the mean lipid percentages in the DRGs and sciatic nerve (SC in Figure S1C). (D) Immunofluorescence analysis of ceramides in primary DRG cultures at different ages of the mice. DAPI was used as nuclear counterstain to assess the cellularity, and neurofilament of 200 kDa (NF200) as a marker of neurons, axons and dendrites

number of autophagolysosomes, similar to the abundance of autophagolysosomes in DRGs of younger mice.[53]

There was also no difference in the ultrastructural morphology of dark neuronal mitochondria (crista type) between *Pink1*$^{-/-}$*SNCA*^{A53T} and wild-type control mice, but some neurons of *Pink1*$^{-/-}$*SNCA*^{A53T} mice were highly packed with very prominent white mitochondria (Figure 4), which do not normally occur in the DRGs of younger mice.[53] The frequency of neurons with such mitochondria was 0%–3.5% in sections of wild-type DRGs and 6%–15% in sections of *Pink1*$^{-/-}$*SNCA*^{A53T} DRGs. These white mitochondria were bloated (higher width Figure 4C) and had fewer or disorganized cristae, reflected by higher brightness (i.e., no structure inside) (Figure 4C). Similar changes of mitochondrial morphology have been previously described in neurons of the cortex and substantia nigra of *Parkin-SNCA* double mutant mice,[54] or mitochondria of neuronal cells exposed to beta-amyloid.[55] Mitochondrial lipidome studies of *Parkin* knockout mice showed elevated levels of some ceramide species.[56] Hence, elevated GlcCer likely contribute to these morphological indices of mitochondrial damage.

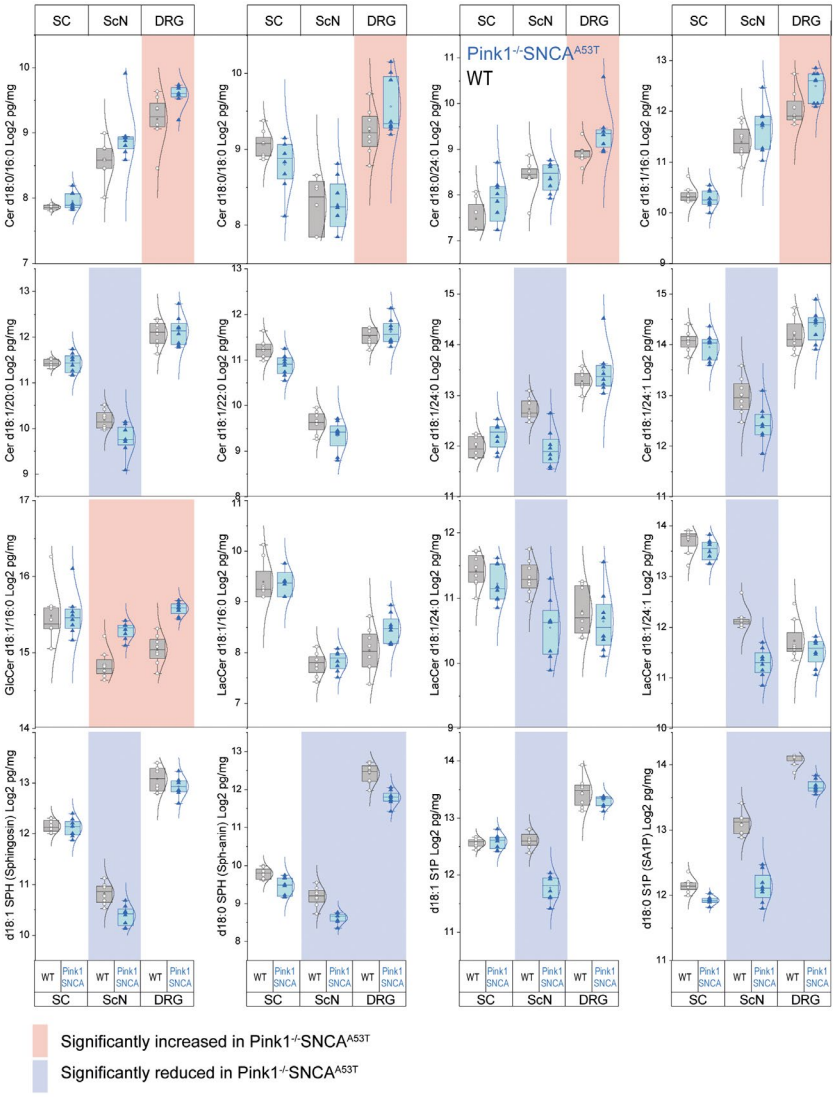

FIGURE 3 Tissue specific analysis of sphingolipid species in DRGs, sciatic nerve and spinal cord. Box/scatter plots show the concentrations of the respective lipids (Y-axes labels) in pg/mg of tissue from spinal cord (SC), sciatic nerve (ScN) and DRGs in 12 months old *Pink1*$^{-/-}$*SNCA*^{A53T} and wild-type control mice (n = 8 per group). Each scatter represents a mouse. The boxes show the interquartile range, the line is the median, the small open circle is the mean, the whiskers show minimum to maximum and the line shows the distribution according to a Gauss fit. Data were compared with two-way ANOVA for each lipid separately, followed by post hoc t tests using an adjustment of alpha according to Holm-Šidák. Lipids and sites with significant differences between genotypes are colour-coded. Red indicates a significant increase and blue a significant decrease

In agreement with this conclusion, accumulation of GlcCer owing to *GBA1* mutations are supposed to interfere with mitochondrial respiration [52] and with the autophagolysosomal removal of damaged mitochondria via mitophagy.[57,58] To assess if pathological mitochondrial morphology was associated with respiratory dysfunction, we measured cellular oxygen consumption and OXPHOS activity with a 'substrate-uncoupler-inhibitor' titration protocol in freshly prepared tissue of the prefrontal cortex, hippocampus and sensory ganglia (DRGs and trigeminal ganglia) in 18 months old *Pink1*$^{-/-}$*SNCA*^{A53T} versus wild-type control mice (Figure 5A exemplary respirograms and Figure 5B quantification). There were no differences between genotypes at the two sites of the brain, but oxygen consumption, Complex-I and C-II respiration and maximum uncoupled respiration were significantly reduced in DRGs of *Pink1*$^{-/-}$*SNCA*^{A53T} mice. The difference was not caused by lower numbers of mitochondria as revealed by normal citrate synthase levels (Figure S2D). The data suggest that sensory neurons of *Pink1*$^{-/-}$*SNCA*^{A53T} mice may suffer from energy deficits and mitochondrial dependent redox stress.

RNA sequencing reveals transcriptional changes in the DRG

To assess if and how mitochondrial pathology was associated with changes at transcriptional levels or reflected by changes of mitochondrial genes, we performed gene expression analyses by RNA sequencing of DRG tissue of prodromal (i.e., "healthy") middle-aged to old mice (Figure 6, leading edge genes in Figure S3, pathways in Figure S4).

Mitochondrial genes or genes involved in mitochondrial biogenesis and transport were similar, but mice clustered perfectly according to genotype by using the 1000 top regulated genes (at 90% confidence level with 1.5-fold change) (Figure 6A). Apart from the knockout of *Pink1*, XY scatter plots (Figure 6A), Volcano (Figure 6B) and MA plots (Figure 6C) revealed a major loss of acidic fibroblast growth factor, *Fgf1* in DRGs of *Pink1*$^{-/-}$*SNCA*^{A53T} mice. FGF1 is known to restore the survival of dopaminergic neurons in PD models,[59,60] and is supportive of developing and postmitotic sensory neurons.[61-65] *Fgf1* is a positive-control gene.

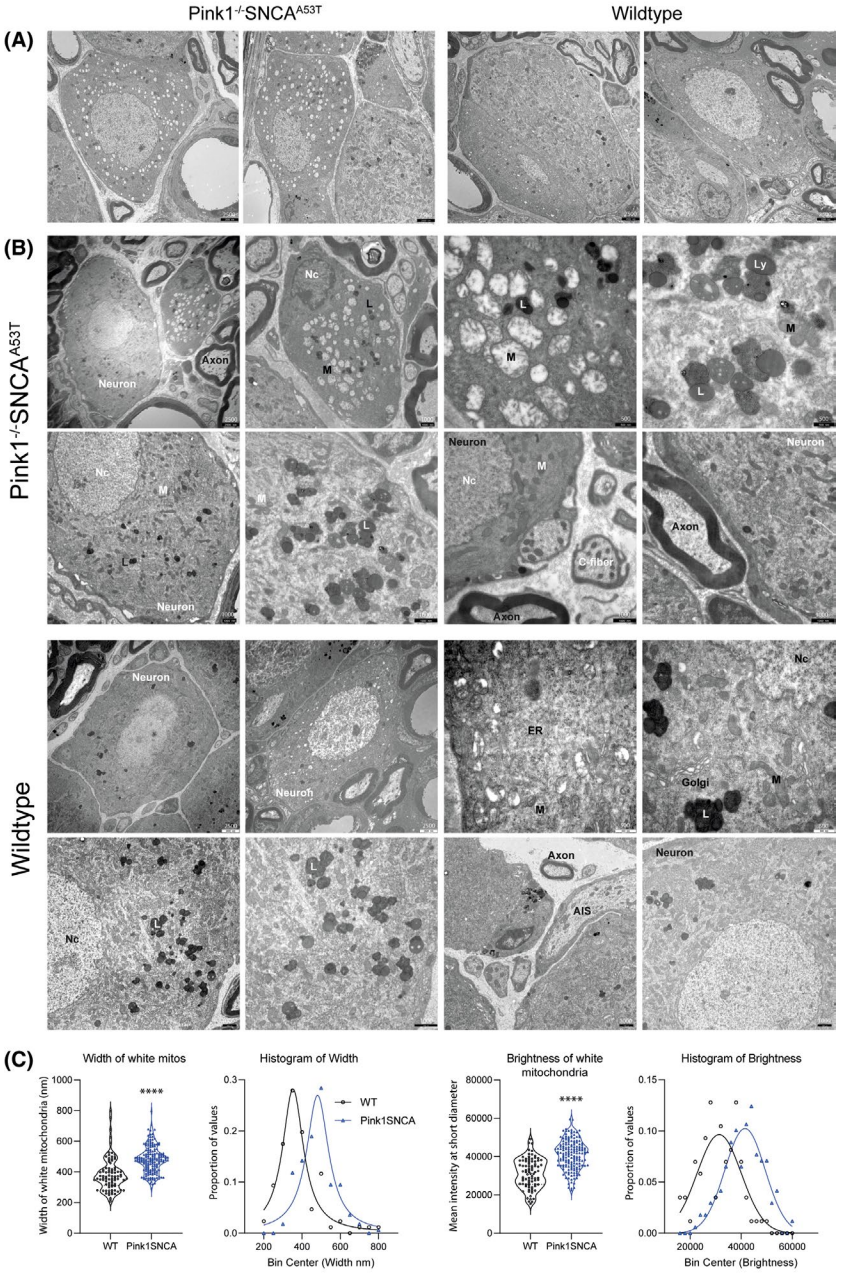

FIGURE 4 Transmission electron microscopy of DRGs and ultrastructural analysis of mitochondria. TEM studies were performed in *Pink1*$^{-/-}$*SNCA*^{A53T} and wild-type control mice at 15–17 months of age, *n* = 3 per genotype, ages matched. (A) Each two examples of neurons with white mitochondria, which were more frequent and prominent in *Pink1*$^{-/-}$*SNCA*^{A53T} mice. These white mitochondria were bloated. (B) The panels show different cell types and organelles in exemplary images of *Pink1*$^{-/-}$*SNCA*^{A53T} and comparable images of wild-type mice. Neurons with dark 'cisterna type' mitochondria did not differ between genotypes. Myelin sheaths, axons, vascular cells and satellite cells did not show overt differences. Prominent lysosomes were present in neurons of both genotypes. AIS, axon initial segment; M, mitochondria; L, lysosome. (C) Quantification of the short diameter of white mitochondria and mean brightness of these mitochondria along the short diameter. High brightness reveals low/no cisternal structure. The width and mean brightness were measured in ImageJ. Please note the higher numbers of white mitochondria in *Pink1*$^{-/-}$*SNCA*^{A53T} DRGs (*n* = 169) than in wild-type mice (*n* = 86), which reflects the higher number of neurons with such mitochondria in *Pink1*$^{-/-}$*SNCA*^{A53T} mice. The data were compared with two-tailed, unpaired Student's *t* tests. ****$p < 0.0001$. The frequency distributions were fitted to a Lorentz (width) and Gauss (brightness) distribution and show a right shift for *Pink1*$^{-/-}$*SNCA*^{A53T}

Further up-regulated genes included *Dnase1l3*, *Ccl27*, *Ccl25*, *Ifi44* and *Il31ra*, pointing to activation of the innate immune system, possibly stimulated by mal-degraded mitochondrial DNA. The immune genes agree with previous microarray studies of the brain where increases of innate immune genes were associated with progressive increases of brain ceramides,[66] hence again pointing to ceramide dysmetabolism. RNAseq data show a down-regulation of ceramidase (*Asah2*) and upregulation of *Cers4*/*LASS4*

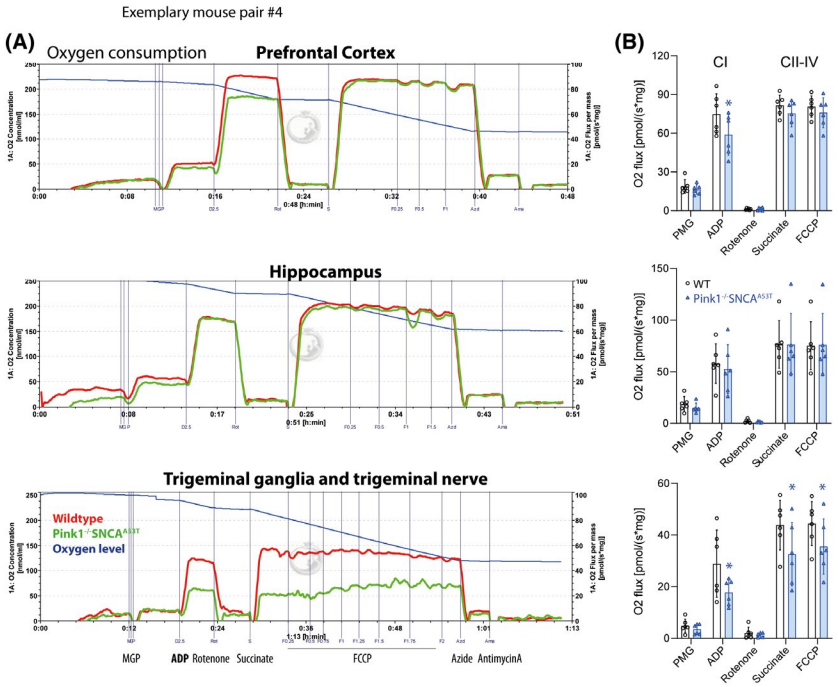

FIGURE 5 Oxygraph respirometry in cortex, hippocampus and trigeminal ganglia. (A) Exemplary respirograms of each one *Pink1*$^{-/-}$*SNCA*^{A53T} and wild-type control mice in freshly prepared homogenates of the prefrontal cortex, hippocampus, and somatosensory ganglia with sensory nerves. (B) Quantitative OXPHOS analysis of six mice per genotype for each site. Mitochondrial respiration was quantified as oxygen flux. LEAK-respiration was induced by adding pyruvate, malate and glutamate (PMG, Complex-I substrates). Complex-I-respiration was initiated by adding ADP in a saturating concentration. To measure C-II respiration, rotenone was added to block C-I, followed by adding succinate. Maximum uncoupled respiration was measured after stepwise titration with the uncoupler, FCCP. Residual oxygen consumption (ROX) was determined after sequential inhibition of complex III with antimycin A and complex IV with azide. Absolute respiration rates were corrected for ROX and normalized for the protein content, and citrate synthase activity was assessed to confirm equivalent numbers of mitochondria (Figure S2D). Data were analysed per two-way ANOVA for repeated measurements (within subject factor "stimulus" versus between subject factor "genotype") and subsequent genotype comparisons for each period using *t* tests with an adjustment of alpha according to Holm- Šidák. Asterisks indicate significant differences between groups, $^{*}p < 0.05$

(ceramide synthase), *Degs1* (desaturase) and *Smpd5* (sphingomyelin phosphodiesterase) (Figure S4) all converging on increases of ceramide levels owing to a combination of mal-metabolism with overproduction.

Gene ontology analyses and gene set enrichment analyses (GSEA) agreed with the top candidate pathways (Figure S4). The major terms, which were enriched in downregulated genes (top 200 down) were "proteolysis", "cell differentiation", and "transmembrane" (mostly receptors). Major terms in upregulated genes (top 200 up) were "nuclease", "immune response", "lipid metabolism" and "ion channel/ion transport". Ion channels determine somatosensory neuron excitability and hence, they were of particular interest for the observed sensory losses. The gene regulations therefore led us to study thermosensitive TRP channels.

Loss of TRP-channels in DRGs and loss of TRPV-calcium signals in sensory neurons of the DRGs

GlcCer overload leads to membrane dysfunction [39] that likely impacts transmembrane ion channels and receptors. The mechanisms are, so far, unknown. Our behavioural studies suggested that thermo-sensory function is particularly vulnerable. Hence, we assessed expression and function of TRP calcium channels that mediate the sensation of heat and cold (Figure 7).

The RNA profile showed a reduction of TRPVs and *TRPA1* and increase of *TRPM6*, whereas redox-sensitive TRPCs were mostly unaffected (Figure 7A). The loss of TRPs was confirmed by RT-PCR (Figure 7B) and immunofluorescence analysis of TRPV1 immunoreactive neurons in DRG sections (Figure 7C counts, Figure 7D exemplary images). Further immunofluorescence studies of the DRGs at 3 and 9 months did not reveal a significant reduction of the numbers of TRPV1 or TRPA1 positive neurons in these younger mice, but TRPM8 was reduced (Figure S5). Hence, the observed loss of thermal sensitivity at the behavioural level preceded the disappearance of the immunofluorescent signal of TRP channels.

There were no differences in gene expression of voltage-gated calcium or sodium channels, but a number of subunits of voltage-gated potassium channels were increased (Figure S4), notably Kv6.3 and Kv6.4, that impact the disease susceptibility of DAergic substantia nigra neurons.[67] Mechanosensitive TREK-1 (*KCNK2*) was not altered (Figure S4), in agreement with the behavioural

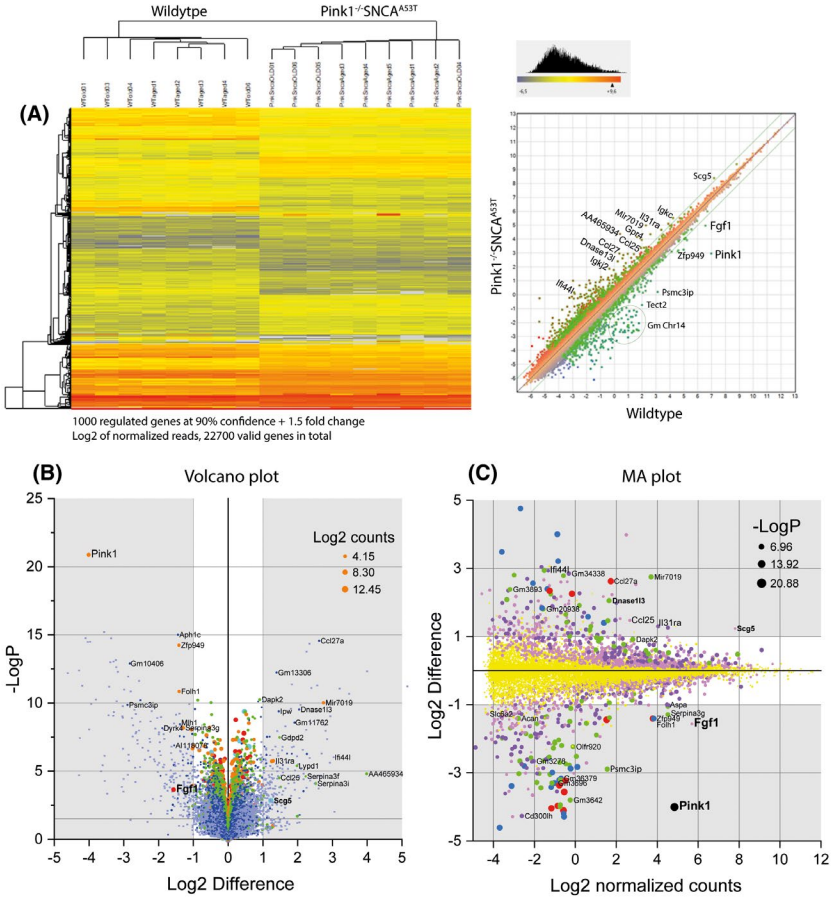

FIGURE 6 Gene expression analysis by RNA sequencing in dorsal root ganglia (DRGs). (A) Heat map of the top 1000 regulated genes and scatter plot of mean normalized counts (Log2) of wild-type control mice (X-axis) and *Pink1*$^{-/-}$*SNCA*^{A53T} mice (Y-axis). Mice were middle aged (10–12 months, n = 4–5 per genotype) and old (18 months, n = 4 per genotype) at the time of tissue preparation. All mice per genotype were analysed together. The green dots in the scatter plot (right) show the genes, which were significant at 90% confidence level plus 1.5 fold change and are represented in the heatmap (left). Mice and genes were clustered according to Euclidean distance metrics. The dendrogram of the mice (on top) shows a clear genotype separation based on differential gene expression. There was no age-dependent structure. (B) Volcano bubble pots showing the Log2 difference of the normalized counts on the X-axis versus the negative logarithm of the p-value of the t test on the Y-axis. The size of the dots and the colour indicates total abundance according to the log2 normalized counts. Hence, the larger the dot, the stronger is the overall expression of the respective gene. Prominent hits are labelled with the gene symbol. (C) MA bubble plots showing log2 normalized counts on the X-axis versus the log2 difference on the Y-axis. The dot size and colour are coded according to the negative logarithm of the p-value of the t test. Hence, the larger the dot, the stronger was the statistical difference between the genotypes. Prominent hits are labelled with the gene symbol. A log2 difference of 1 shows a 2-fold change

data, where paw withdrawal upon mechanical stimulation was in the normal range.

To assess the functional implications of TRP channel changes, primary DRG neurons of 18 months old *Pink1*$^{-/-}$*SNCA*^{A53T} and wild-type mice were stimulated with capsaicin to activate TRPV1 and formalin to activate TRPA1. It is of note that the immunofluorescent morphology of neurons, dendrites and growth cones was alike in *Pink1*$^{-/-}$*SNCA*^{A53T} and wild-type DRG cultures (Figure S6A). Immunofluorescence studies also did not reveal overt differences of autophagy, protein aggregates, or membrane and ER markers (Figure S6B).

Calcium influx in DRG neurons was determined as Fura2 absorbance ratios from 300 to 350 neurons per group and stimulus. High-K+ responsive neurons (80%–90% in each culture) were used for group comparisons (Figure 7E–H). Time courses of [Ca^{2+}]i (Figure 7E,G) and violin plots of the areas under the curve (AUC) (Figure 7F,H) revealed lower peak calcium influx and reduced net increases upon stimulation in *Pink1*$^{-/-}$*SNCA*^{A53T} DRGs. The responses of *Pink1*$^{-/-}$*SNCA*^{A53T} DRG neurons were more heterogeneous than WT neurons and showed a triple-phasic distribution upon stimulation with capsaicin or formalin representing non-responding, low-responding and high-responding neurons. Similarly, a double peak distribution upon high-K^+ contrasted with the mono-phasic distribution of the wild-type neurons and revealed that about half of the *Pink1*$^{-/-}$*SNCA*^{A53T} neurons had abnormally low depolarization-evoked calcium fluxes.

The data suggest that a loss of TRP channel function and abundance leads to the observed thermal sensory loss at the behavioural

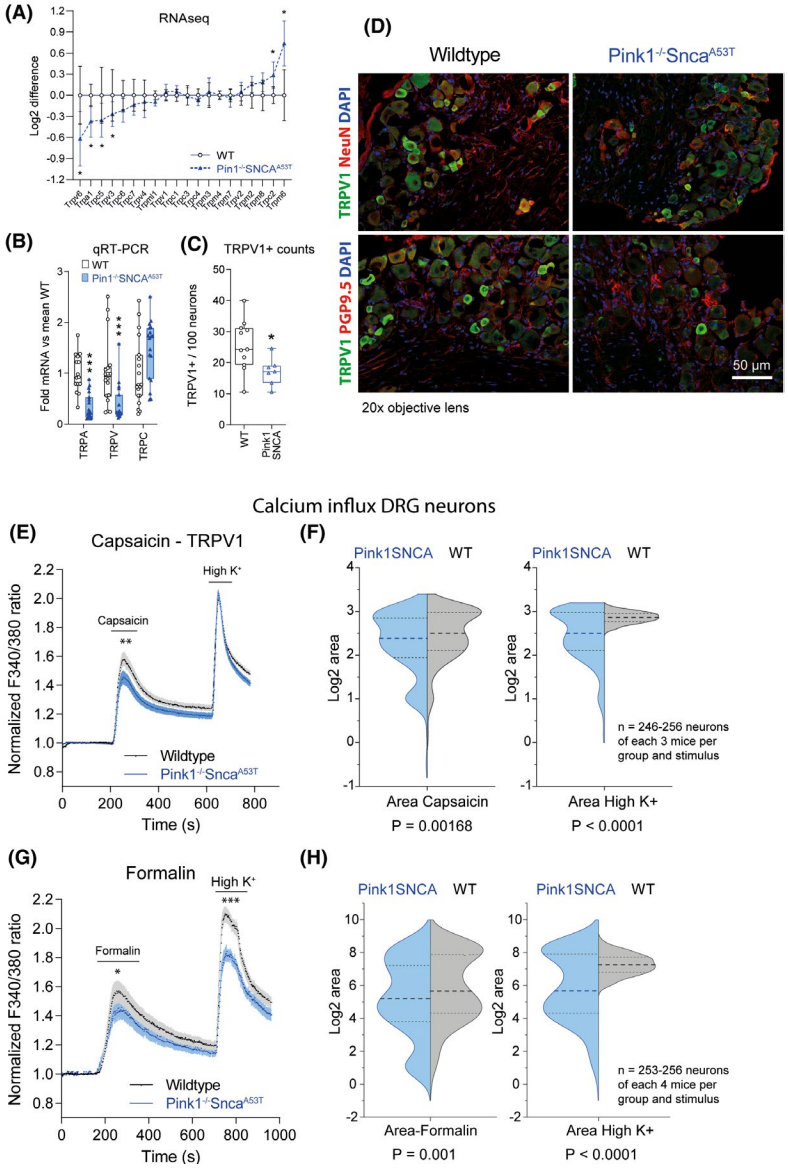

FIGURE 7 Calcium imaging and expression of TRP channels in DRGs. (A) RNA sequencing results of TRP channel expression in DRGs (mice as explained in Figure 7). For comparison, the reads were normalized to the mean log2 counts of wild-type control mice, and they are expressed as the log2 difference. Data were compared per two-way ANOVA and multiple comparisons corrected for the False Discovery Rate (FDR) according to Benjamini, Krieger and Yekutieli. Asterisks indicate multiplicity adjusted *p* values, $*p < 0.05$. (B) Quantitative rt-PCR analysis of TRP channel gene expression in DRGs of *Pink1*$^{-/-}$*SNCA*^{A53T} and wild-type control mice, which were 7 months (each group $n = 7$) and 16–18 months old (each group $n = 4$). Each scatter represents a mouse. Expression of each TRP channel was analysed per 2-tailed, unpaired Student's *t* test. Different ages were pooled. (C, D) Immunofluorescence analysis of TRPV1 expression in DRGs of *Pink1*$^{-/-}$*SNCA*^{A53T} and wild-type control mice at 18 months of age. Each two exemplary images in D, quantification in C. Each scatter represents a complete DRG slice obtained from stitched images, counts are from 3 to 4 mice per group. (E) Time course of calcium influx in primary DRG neurons of *Pink1*$^{-/-}$*SNCA*^{A53T} and wild-type control mice on stimulation with capsaicin (1 µM from 180 to 206 s) to stimulate TRPV1 channels and with high K^+ (100 mM KCl, from 600 to 630 s) to evoke depolarization-evoked calcium currents. Data are means ± SEM of 246 and 256 neurons (*Pink1*$^{-/-}$*SNCA*^{A53T} and WT) of 10–12 cultures of each 3 mice per group, which were 18 months old. All neurons responding to high K^+ with >1.5-fold increase of $[Ca^{2+}]i$ (viable neurons) were included in the analysis. Calcium fluxes were determined as absorbance ratio of Fura2 at excitation wavelengths of 340 and 380 nm. Ratios were normalized to the mean baseline ratio, set to 1. (F) Half violin plots of the log2-transformed areas under the peak calcium versus time curves (AUCs) of the neurons shown in E. AUCs were determined by integration from 198 to 500 s for capsaicin and 600–778 s for high K^+. The thick dashed line shows the median, the dotted lines show the interquartile range. The violin shows the distribution, obtained by Kernel density estimation. (G) In analogy to E, time courses of calcium influx upon stimulation of DRG neurons with formalin (0.01% from 100 to 200 s) to stimulate TRPA1 channels and with high K+ (100 mM KCl from 680 to 780 s). Data are means ±sem of 253 and 256 neurons (*Pink1*$^{-/-}$*SNCA*^{A53T} and WT) of 12–14 cultures of each four mice per group. Mice were 18 months old. (H) In analogy to F, half violin plots show Log2 transformed AUCs of neurons presented in C. AUCs were determined by integration from 175 to 520 s for formalin and 695–950 s for high K^+. Peaks and AUCs were compared with two-sided, unpaired *t* tests, time courses by two-way ANOVA. $*p < 0.05$, $**p < 0.001$, $***p < 0.0001$

level. It is conceivable that high levels of GlcCer directly interfere with the gating properties and membrane insertion of TRP channels. TRPs crucially depend on membrane lipid composition.[68-70]

Glucosylceramides lead to hyperexcitability of primary sensory neurons

To address the direct effects of GlcCer on neuronal structure and TRP channel function, DRG cultures were treated with GlcCer24:1. Short-term treatment (24–48 h) had no effect on the morphology or outgrowth dynamics of the dendritic trees up to 10 µM GlcCer24:1 (Figures S7 and S8). Viability in the first 2 days was not impaired, as assessed by the fraction of neurons responding to "high-K^+" with a minimum 1.5-fold increase in $[Ca^{2+}]i$ (Figure 8A top). About one-third of viable neurons responded to capsaicin stimulation in both groups (Figure 8A, bottom), and these neurons were used for further analyses.

Capsaicin-responsive neurons carry functional TRPV1 receptors and are nociceptive. Individual calcium traces from these neurons are shown in Figure 8B. The time courses of the calcium influx evoked by capsaicin perfusion (yellow marked period) and on depolarization (green marked period) reveal that calcium influx was increased in GluCer24:1 pre-treated neurons. Statistically, this is demonstrated by comparisons of the areas under the calcium influx versus time curves (AUCs) and the peak calcium influx (Figure 8C). AUCs and peaks differed and were significantly higher in GluCer24:1 treated neurons (unpaired, 2-sided *t* tests).

Glucosylceramides reduce sensory neuron longevity

To assess the impact on culture longevity upon protracted GlcCer24:1 treatment, live cultures were captured daily and the coverage with neuronal bodies and neurites was analysed. The statistical analysis in Figure 8D revealed a premature decline of culture density in GlcCer24:1 treated cultures suggesting a negative impact of GlcCer24:1 on sensory neuron longevity, exemplified by a culture profile plot (Figure 8E) that reveals the rarefication of neuronal somata at 96 h. Exemplary time courses of culture images are in Figure S9A and quantification of neuronal numbers in Figure S9B.

Overall, the *in vitro* data shows that GlcCer24:1 causes hyperexcitability following short-term treatment of sensory neurons, presumably owing to membrane instability, which may ultimately result in calcium overload, mitochondrial damage, redox stress and premature damage of highly vulnerable thermosensitive neurons, which is reflected both in the mouse and the human phenotype of PD-associated sensory neuropathy.

DISCUSSION

Somatosensory neuropathies are a frequent manifestation of PD, and the onset is often years before the occurrence of motor dysfunction.[16] The high vulnerability of sensory neurons in PD is not well-understood. In contrast with olfactory sensory neurons, which are also affected early in the course of PD, only a few neurons of the dorsal root ganglia are dopaminergic.[71]

We show in the present study that *Pink1*$^{-/-}$*SNCA*^{A53T} double mutant mice phenocopy the human prodromal sensory neuropathy. These mice give new insight into the pathogenic events that culminate in an early PD-associated sensory neuropathy. They show a progressive loss of thermal sensation starting far earlier than the earliest occurrence of clinical motor dysfunction. The sensory phenotype is reminiscent of the QST phenotype of PD patients that is characterized by a predominant loss of thermal sensation with/without mechanical hypersensitivity.[18,72] Thermal sensation relies on TRPV positive DRG neurons [73,74] and non-myelinated C-fibres,[75] whereas mechanosensation is mediated primarily through myelinated neurons with A-delta fibres.[76] The phenotype suggests distinct vulnerabilities of these subsets of sensory neurons.

At the transmission microscopy level, we did not detect overt morphological signs of neuronal death or damage in DRGs of *Pink1*$^{-/-}$*SNCA*^{A53T} mice. However, studies in PD patients show that the density of sensory fibre terminals in the skin is reduced,[15,72] reminiscent of small fibre polyneuropathies in metabolic diseases [77] suggesting that metabolic deregulation may contribute to the sensory decline in PD, possibly involving lipids. Indeed, in PD patients, sensory loss and pain intensity ratings are associated with high levels of plasma glucosylceramides.[8]

In agreement with the human data, we show now that GlcCer accumulate in the DRGs of *Pink1*$^{-/-}$*SNCA*^{A53T} mice suggesting that GlcCer are not only biomarkers but have a pathogenic role in neuropathy and neuropathic pain. GlcCer treatment of primary DRG neurons resulted in a hyperexcitability of subsets of neurons and premature aging of neuronal cultures after prolonged exposure. This duality recapitulates the clinical phenotype where sensory loss is often associated with burning pain. It is not clear, how GlcCer affect ion channel properties. So far, most studies addressing the functional consequences of *GBA1* deletion assumed that the observed pathology was caused by glucosylceramides without directly measuring these lipids. It was reported that *GBA1* deletion or mutation increases alpha-synuclein aggregates,[28,29] leads to mitochondrial calcium overload,[58] ER stress [78] and disruption of autophagolysosomal pathways [79] (Graphical illustration in Figure 9). It is of note that Gaucher disease may manifest with a sensory neuropathy in some patients [80] but is not a predominant feature, possibly because of the younger age as compared to sporadic PD and the polygenetic nature of PD. Disease manifestations in *Pink1*$^{-/-}$*SNCA*^{A53T} are likely a function of “genes x GlcCer x age”.

In Gaucher disease, a metabolite of GlcCer, glycosylsphingosine (GlcSph), rather than GlcCer itself, was postulated to be a biomarker for disease progression.[81,82] Both, GlcCer and their metabolites, glucosyl- and galactosyl-sphingosines (psychosines) were shown to disrupt mitochondrial membranes and oxidative phosphorylation.[83,84] In line with these mechanistic reports, our ultrastructural and OXPHOS studies show that subsets of neurons have high numbers

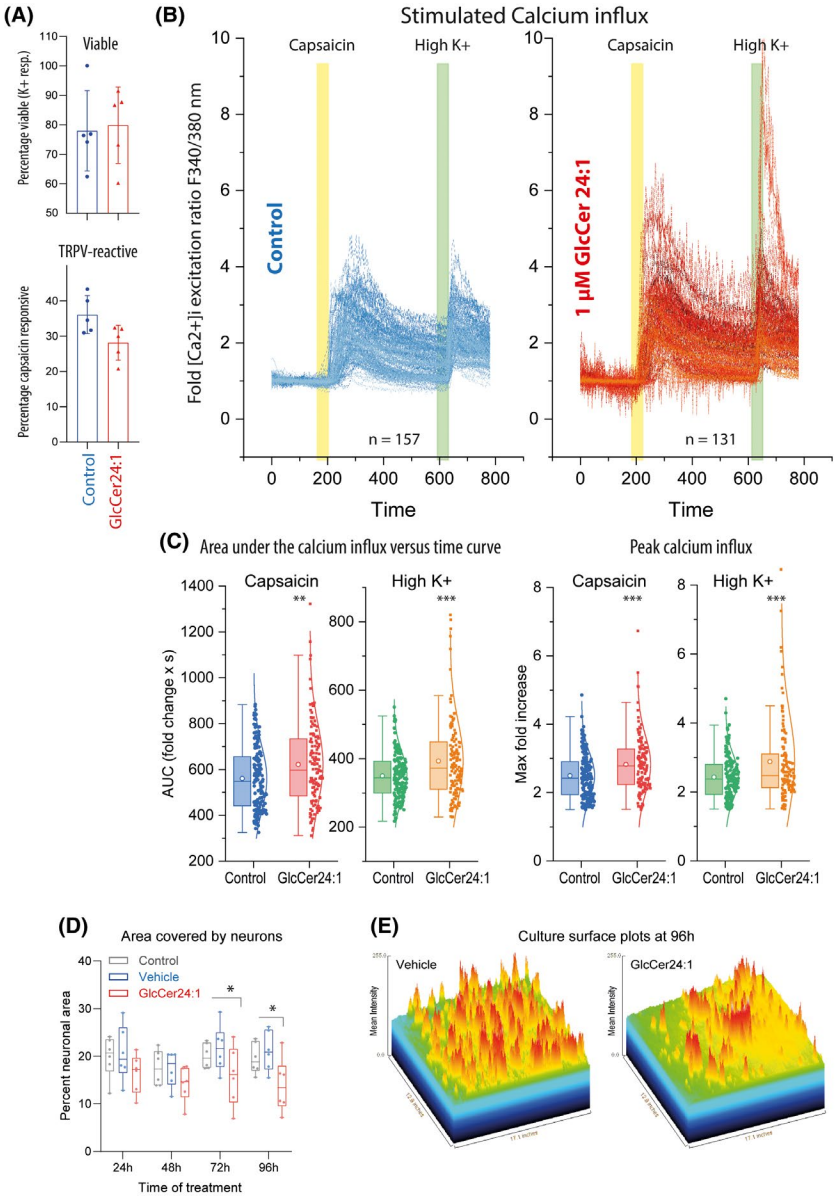

FIGURE 8 Calcium fluxes in primary DRG neurons treated with GlcCer24:1 for 24 h and culture viability. Primary DRG neuron cultures were prepared from adult C57BL6 mice (n = 5 mice, each with 6/6 cultures) for treatment with 1 µM GlcCer24:1 versus vehicle for 24 h. Treatments started one or 2 days after plating. In total, n = 591 and n = 594 neurons were captured for GlcCer24:1 and control neurons, respectively. About 90% were viable and responded to high K^+. (A) The bar/scatter plot shows the relative frequency of high K^+ responsive viable neurons out of all neurons (top), and the frequency of capsaicin responsive neurons out of the viable neurons (bottom), from five independent sequential experiments. *p < 0.05, independent, two-sided t test. (B) Line graphs show the individual neuron time courses of $[Ca^{2+}]_i$, calculated as absorbance ratio of Fura-2 at excitation ratios of 340 and 380 nm. Capsaicin perfusion was from 180 to 206 s after start (yellow marked area), and KCl from 600 to 630 s (green marked area). (C) Box/scatter plots and Gauss distributions of the areas (AUC) and maxima of capsaicin evoked calcium influx and of high K^+ evoked calcium influx. The areas were calculated from 180 to 500 s for capsaicin and 550–780 s for high K^+. The box is the interquartile range, the line is the median, the open circle is the mean, whiskers show minimum to maximum. The scatters are neurons. Areas and maxima were compared with independent, two-sided t tests for each stimulus. The analysis included n = 159 and n = 131 neurons in control and GlcCer24:1 cultures. The cultures were from five mice per treatment. The asterisks indicate significant differences between groups, **p < 0.001, ***p < 0.0001. (D) For long-term exposure, cultures were treated with 1 µM GlcCer daily. Half of the medium was replaced with fresh medium containing 1 µM. Hence, concentrations in the cultures increased by 50% each day. Images of live cultures were captured daily (exemplary images are shown in Figure S7). Tiled images were stitched to observe all neurons. The coverage of the cover slips with neuronal bodies and dendrites was assessed in binarized images in FIJI ImageJ. The density of the cultures (box/scatter plots) declined in GlcCer24:1 conditions at 72 and 96 h; 2-way ANOVA for "time" X "treatment" and subsequent t test for "treatment" with adjustment of alpha according to Šidák. *adjusted p < 0.05. (E) Exemplary culture 3D surface plots of 96 h cultures treated with GlcCer24:1 versus vehicle. The intensity ranges from blue (cover slip bottom without growth) to high intensity (red) of neuronal bodies (rainbow colours). Red peaks represent the neuronal somata. The low number of the red crests in the GlcCer24:1 culture shows the thinning of the neuronal culture

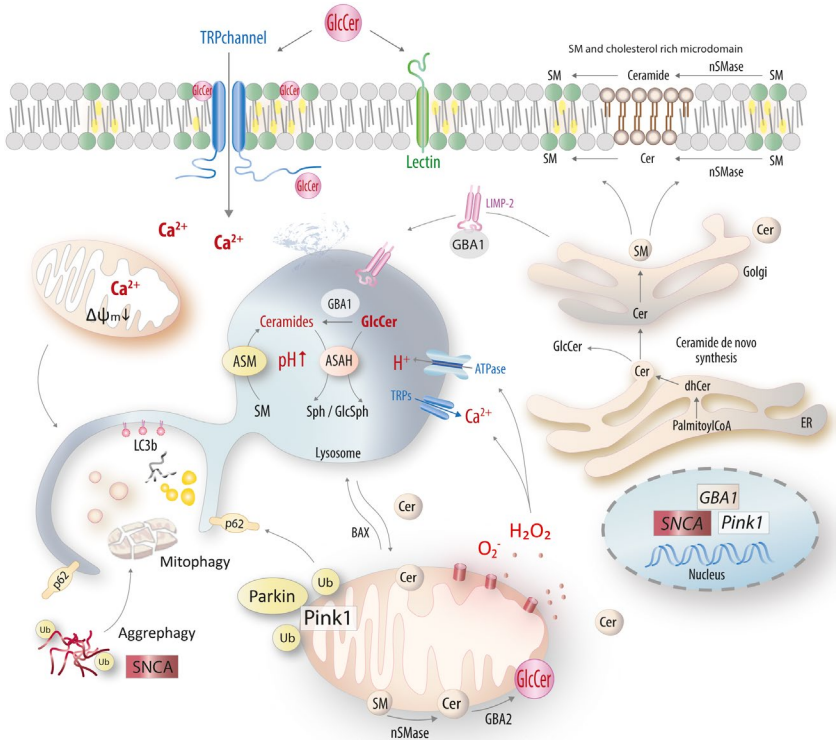

FIGURE 9 Putative signalling paths of GlcCer in PD-associated pathology. *Pink1* deficiency and mutant *SNCA* cause genetic PD, and mutations of *GBA1* are associated with sporadic PD. The enzyme glucocerebrosidase, GBA1 is needed for degradation of glucosylceramides (GlcCer). The graph illustrates how elevated GlcCer may initiate or further aggravate PD-associated pathology of mitochondria, lysosomes and membranes. Ceramides and GlcCer are essential components of membranes, required for membrane fluidity, the composition of lipid rafts and functioning of transmembrane ion channels like TRP channels. Membrane ceramides are generated in membranes via neutral sphingomyelinase (nSMase) on demand, and GlcCer are inserted into the outer leaflet of the plasma membrane. The compartmentalized homeostasis of membrane ceramides and GlcCer is disrupted upon overload with these lipids, which may lead to hyperexcitability or loss of TRP channels. GlcCer are degraded via GBA1, an acidic lysosomal enzyme that is transferred from the ER to the lysosome via LIMP2. Malfunction of GBA1 can arise from mal-transport, mutation, high pH or calcium overload. The resulting accumulation of glycosphingolipids further disrupts membrane charge, acidification, enzyme functions, lysosomal membrane integrity and autophagolysosomal flux. Autophagolysosomal degradation is the major pathway for removal of SNCA aggregates and of defective mitochondria via mitophagy. Mitophagy depends on Pink1-Parkin mediated ubiquitin labelling of the mitochondrial membrane. GlcCer overload promotes the aggregation of SNCA and may aggravate the failure of mitophagy, leading to a release of Bax and oxidative species (ROS). ROS further compromise lysosomal ATPase and TRP channels, leading to further accumulation of sphingolipids and calcium overload. Δψm, depolarization of mitochondrial transmembrane potential; ASM, acidic sphingomyelinase; ASAH, acid ceramidase; Cer, ceramides; dhCer, dihydro-ceramides; ER, endoplasmic reticulum; GBA1, GBA2 glucocerebrosidase alpha and beta; GlcCer, glucosylceramides; GlcSph, glucosylsphingosines; LIMP2, lysosomal integral membrane protein; Pink1, PTEN induced kinase; SM, sphingomyelin; SMase, sphingomyelinase; SNCA, alpha synuclein; Sph, Sphingosine; TRP channel, transient receptor potential channel; Ub, ubiquitin

of white mitochondria that do not normally occur at younger age and were associated with respiratory dysfunction.

The mitochondria had a bloated appearance with partially disrupted cristae, and these morphological abnormalities bear some resemblance to those described in human PD patients' brains.[85-87] Mitochondria are susceptible to morphological EM artefacts but we did not observe swollen mitochondria in DRGs in younger mice in a previous technically identical study,[53] and swollen mitochondria were consistently more abundant in *Pink1*$^{-/-}$*SNCA*^{A53T} mice than in controls and were only evident in specific neurons. Owing to the genetic defect of *Pink1*, we assume that damaged mitochondria were not efficiently removed by mitophagy.[88-90]

Although there was no ultrastructural pathology of autophagolysosomes, lysosomal pathology likely contributed to the pathology because glycosphingolipids act as detergents on lysosomal membranes and disrupt the function of lysosomal enzymes. The functioning of GBA1 depends on folding and proper transfer from the ER to the lysosomes, a process that requires transport via the lysosomal integral membrane protein-2, LIMP2,[91,92] lysosomal acidic pH, negative membrane charge and negative calcium gradients [93] (Graphical illustration Figure 9). Intralysosomal calcium is kept low via outward calcium transport through TRP channels,[94,95] which is impaired by accumulating lipids.[96] It is of note that GBA1 dysfunction increases neuronal sensitivity towards calcium overload.[58] GlcCer accumulation, membrane instability and calcium

overload likely coincide or converge on axonal damage and loss of nerve terminals. Considering that heterozygous *GBA1* mutations are the strongest independent risk factor for sporadic PD, we assume that GlcCer accumulation occurs early in the course of the disease and leads to mitochondrial damage and channel dysfunction.

Heat-evoked calcium influx in somatosensory neurons is mediated through TRPV channels. They are regulated by phosphorylation, redox modification, calmodulin and clathrin-mediated endocytosis.[69,97-101] TRP channels are also sensitive to lipid-mediated modification, including phosphoinositides [68,69,102] and oxidized linoleic acid metabolites.[103,104] It is conceivable that GlcCer directly change the gating properties or interfere with the desensitization of TRP channels. We observed an exaggerated calcium influx in GlcCer-treated cultures, which was not specific for TRPV1 stimulation, but also occurred upon depolarization pointing to membrane instability in agreement with an *in vitro* Gaucher model, where sphingolipid accumulation made plasma membranes more pliable.[105]

To stop progression of neurodegeneration, one would like to know the causal chain of pathophysiological events. From the genetics of *Pink1*$^{-/-}$*SNCA*^{A53T} mice, we expected SNCA aggregates and defective mitophagy. Indeed, we observed bloated dysfunctional mitochondria. GlcCer accumulation likely aggravates the failure of mitophagy because of the disruption of lysosomal functions. Incomplete removal of damaged mitochondria results in oxidative stress and activation of innate immune responses,[26,106,107] which occurs concurrently with ceramide accumulation in the aging *Pink1*$^{-/-}$*SNCA*^{A53T} brain.[66]

Based on the *Pink1*$^{-/-}$*SNCA*^{A53T} double mutant phenotype and the combined GlcCer and mitochondrial pathology, we propose that GlcCer accumulation results in membrane instability and mitochondrial membrane disruption, and hyperexcitability leads to calcium overload with subsequent secondary damage, ultimately converging on a loss of sensory nerve terminals. We have evaluated multiple mechanistic aspects, which contribute to the prodromal sensory loss in *Pink1*$^{-/-}$*SNCA*^{A53T} mice. There is no single gene or pathway acting as single disease operator, but pathological events coincide and converge on small fibre neuropathy. The combined deregulation of sphingolipid metabolism, TRP channel dysfunction and loss and mitochondrial damage most convincingly explained the behavioural phenomena of early prodromal somatosensory loss and PD-associated pain. Because of the very early onset, QST for heat sensitivity may allow for early diagnosis, and pharmacological manipulation of GlcCer metabolic pathways may offer novel therapeutic options.

ACKNOWLEDGEMENTS

We thank Anke Biczysko for excellent technical assistance in ultrastructural analyses.

CONFLICT OF INTEREST

The authors declare that there are no conflicts of interest. The funding institution had no role in data acquisition, analysis or decision to publish the results.

AUTHOR CONTRIBUTIONS

LV performed the behavioural studies, immunofluorescence and EM analyses with tissues and primary cultures, calcium imaging experiments and analysed data. BT performed behavioural studies. AWS did the RNAseq experiments and organized mice. JH performed the mitochondrial function tests. TS and BB provided assistance of RNAseq experiments. GA generated the *Pink1*$^{-/-}$*SNCA*^{A53T} double mutant mice and discussed data. ST analysed lipids by LC-MS/MS, and DT and GG organized and managed the lipid analysis lab. TD provided EM knowledge and discussed data. IT initiated the study, supervised the studies, analysed calcium imaging, immunofluorescence and omics data, drafted the manuscript and made the figures. All authors contributed to drafting or editing of parts of the manuscript and approved the final version of the manuscript. All authors read and approved the final manuscript.

AVAILABILITY OF SUPPORTING DATA

RNA sequencing data have been deposited at GEO datasets with the provisional accession GSE146091. Other supporting data are included as Data S1.

ETHICAL APPROVAL

The experiments were approved by the local Ethics Committee for animal research (Darmstadt, Germany), adhered to the guidelines for pain research in conscious animals of the International Association for the Study of PAIN (IASP) and those of the Society of Laboratory Animals (GV-SOLAS) and were in line with the European and German regulations for animal research.

PEER REVIEW

The peer review history for this article is available at https://publons.com/publon/10.1111/nan.12734.

ORCID

Irmgard Tegeder https://orcid.org/0000-0001-7524-8025

REFERENCES

1. Darweesh SK, Verlinden VJ, Stricker BH, Hofman A, Koudstaal PJ, Ikram MA. Trajectories of prediagnostic functioning in Parkinson's disease. *Brain*. 2017;140:429-441.
2. Braak H, Braak E, Yilmazer D, Schultz C, de Vos RA, Jansen EN. Nigral and extranigral pathology in Parkinson's disease. *J Neural Transm Suppl*. 1995;46:15-31.
3. Schrag A, Horsfall L, Walters K, Noyce A, Petersen I. Prediagnostic presentations of Parkinson's disease in primary care: a case-control study. *Lancet Neurol*. 2015;14:57-64.
4. Rana AQ, Siddiqui I, Mosabbir A, et al. Association of pain, Parkinson's disease, and restless legs syndrome. *J Neurol Sci*. 2013;327:32-34.
5. Berardelli A, Wenning GK, Antonini A, et al. EFNS/MDS-ES/ENS [corrected] recommendations for the diagnosis of Parkinson's disease. *Eur J Neurol*. 2013;20:16-34.
6. Postuma RB, Aarsland D, Barone P, et al. Identifying prodromal Parkinson's disease: pre-motor disorders in Parkinson's disease. *Mov Disord*. 2012;27:617-626.
7. Snider SR, Fahn S, Isgreen WP, Cote LJ. Primary sensory symptoms in parkinsonism. *Neurology*. 1976;26:423-429.

8. Klatt-Schreiner K, Valek L, Kang JS, et al. High glucosylceramides and low anandamide contribute to sensory loss and pain in Parkinson's disease. *Mov Disord*. 2020;35(10):1822-1833.
9. Djaldetti R, Yust-Katz S, Kolianov V, Melamed E, Dabby R. The effect of duloxetine on primary pain symptoms in Parkinson disease. *Clin Neuropharmacol*. 2007;30:201-205.
10. Djaldetti R, Shifrin A, Rogowski Z, Sprecher E, Melamed E, Yarnitsky D. Quantitative measurement of pain sensation in patients with Parkinson disease. *Neurology*. 2004;62:2171-2175.
11. Yust-Katz S, Hershkovitz R, Gurevich T, Djaldetti R. Pain in extrapyramidal neurodegenerative diseases. *Clin J Pain*. 2017;33:635-639.
12. Leclair-Visonneau L, Magy L, Volteau C, et al. Heterogeneous pattern of autonomic dysfunction in Parkinson's disease. *J Neurol*. 2018;265:933-941.
13. Zambito Marsala S, Tinazzi M, Vitaliani R, et al. Spontaneous pain, pain threshold, and pain tolerance in Parkinson's disease. *J Neurol*. 2011;258:627-633.
14. Kass-Iliyya L, Javed S, Gosal D, et al. Small fiber neuropathy in Parkinson's disease: a clinical, pathological and corneal confocal microscopy study. *Parkinsonism Relat Disord*. 2015;21:1454-1460.
15. Nolano M, Provitera V, Estraneo A, et al. Sensory deficit in Parkinson's disease: evidence of a cutaneous denervation. *Brain*. 2008;131:1903-1911.
16. Zis P, Grunewald RA, Chaudhuri RK, Hadjivassiliou M. Peripheral neuropathy in idiopathic Parkinson's disease: a systematic review. *J Neurol Sci*. 2017;378:204-209.
17. Nolano M, Provitera V, Manganelli F, et al. Loss of cutaneous large and small fibers in naive and l-dopa-treated PD patients. *Neurology*. 2017;89(8):776-784.
18. Strobel AV, Tankisi H, Finnerup NB, et al. Somatosensory function is impaired in patients with idiopathic REM sleep behaviour disorder. *Sleep Med*. 2018;42:83-89.
19. Silverdale MA, Kobylecki C, Kass-Iliyya L, et al. A detailed clinical study of pain in 1957 participants with early/moderate Parkinson's disease. *Parkinsonism Relat Disord*. 2018;56:27-32.
20. Pont-Sunyer C, Hotter A, Gaig C, et al. The onset of nonmotor symptoms in Parkinson's disease (the ONSET PD study). *Mov Disord*. 2015;30:229-237.
21. Rey NL, Steiner JA, Maroof N, et al. Widespread transneuronal propagation of alpha-synucleinopathy triggered in olfactory bulb mimics prodromal Parkinson's disease. *J Exp Med*. 2016;213:1759-1778.
22. Bernis ME, Babila JT, Breid S, Wusten KA, Wullner U, Tamguney G. Prion-like propagation of human brain-derived alpha-synuclein in transgenic mice expressing human wild-type alpha-synuclein. *Acta Neuropathol Commun*. 2015;3:75.
23. Loria F, Vargas JY, Bousset L, et al. alpha-Synuclein transfer between neurons and astrocytes indicates that astrocytes play a role in degradation rather than in spreading. *Acta Neuropathol*. 2017;134:789-808.
24. Peelaerts W, Bousset L, Van der Perren A, et al. alpha-Synuclein strains cause distinct synucleinopathies after local and systemic administration. *Nature*. 2015;522:340-344.
25. Blanz J, Saftig P. Parkinson's disease: acid-glucocerebrosidase activity and alpha-synuclein clearance. *J Neurochem*. 2016;139(Suppl 1):198-215.
26. Sliter DA, Martinez J, Hao L, et al. Parkin and PINK1 mitigate STING-induced inflammation. *Nature*. 2018;561:258-262.
27. Suzuki M, Sango K, Wada K, Nagai Y. Pathological role of lipid interaction with alpha-synuclein in Parkinson's disease. *Neurochem Int*. 2018;119:97-106.
28. Kim S, Yun SP, Lee S, et al. GBA1 deficiency negatively affects physiological alpha-synuclein tetramers and related multimers. *Proc Natl Acad Sci USA*. 2018;115:798-803.
29. Zunke F, Moise AC, Belur NR, et al. Reversible conformational conversion of alpha-synuclein into toxic assemblies by glucosylceramide. *Neuron*. 2018;97:92-107.e10.
30. Murphy KE, Gysbers AM, Abbott SK, et al. Reduced glucocerebrosidase is associated with increased alpha-synuclein in sporadic Parkinson's disease. *Brain*. 2014;137:834-848.
31. Tayebi N, Parisiadou L, Berhe B, et al. Glucocerebrosidase haploinsufficiency in A53T alpha-synuclein mice impacts disease onset and course. *Mol Genet Metab*. 2017;122:198-208.
32. Suzuki M, Fujikake N, Takeuchi T, et al. Glucocerebrosidase deficiency accelerates the accumulation of proteinase K-resistant alpha-synuclein and aggravates neurodegeneration in a Drosophila model of Parkinson's disease. *Hum Mol Genet*. 2015;24:6675-6686.
33. Abul Khair SB, Dhanushkodi NR, Ardah MT, Chen W, Yang Y, Haque ME. Silencing of glucocerebrosidase gene in drosophila enhances the aggregation of Parkinson's disease associated alpha-synuclein mutant A53T and affects locomotor activity. *Front Neurosci*. 2018;12:81.
34. Migdalska-Richards A, Wegrzynowicz M, Rusconi R, et al. The L444P Gba1 mutation enhances alpha-synuclein induced loss of nigral dopaminergic neurons in mice. *Brain*. 2017;140:2706-2721.
35. Do J, McKinney C, Sharma P, Sidransky E. Glucocerebrosidase and its relevance to Parkinson disease. *Mol Neurodegener*. 2019;14:36.
36. Alcalay RN, Levy OA, Waters CC, et al. Glucocerebrosidase activity in Parkinson's disease with and without GBA mutations. *Brain*. 2015;138:2648-2658.
37. Murphy KE, Halliday GM. Glucocerebrosidase deficits in sporadic Parkinson disease. *Autophagy*. 2014;10:1350-1351.
38. Robak LA, Jansen IE, van Rooij J, et al. Excessive burden of lysosomal storage disorder gene variants in Parkinson's disease. *Brain*. 2017;140:3191-3203.
39. Schulze H, Sandhoff K. Lysosomal lipid storage diseases. *Cold Spring Harb Perspect Biol*. 2011;3.
40. Ishibashi Y, Kohyama-Koganeya A, Hirabayashi Y. New insights on glucosylated lipids: metabolism and functions. *Biochim Biophys Acta*. 2013;1831:1475-1485.
41. Perez-Lloret S, Rey MV, Dellapina E, Pellaprat J, Brefel-Courbon C, Rascol O. Emerging analgesic drugs for Parkinson's disease. *Expert Opin Emerg Drugs*. 2012;17:157-171.
42. Sophie M, Ford B. Management of pain in Parkinson's disease. *CNS Drugs*. 2012;26:937-948.
43. Valek L, Auburger G, Tegeder I. Sensory neuropathy and nociception in rodent models of Parkinson's disease. *Dis Model Mech*. 2019;12:dmm039396.
44. Gispert S, Brehm N, Weil J, et al. Potentiation of neurotoxicity in double-mutant mice with Pink1 ablation and A53T-SNCA overexpression. *Hum Mol Genet*. 2015;24:1061-1076.
45. Touska F, Winter Z, Mueller A, Vlachova V, Larsen J, Zimmermann K. Comprehensive thermal preference phenotyping in mice using a novel automated circular gradient assay. *Temperature*. 2016;3:77-91.
46. Valek L, Haussler A, Drose S, Eaton P, Schroder K, Tegeder I. Redox-guided axonal regrowth requires cyclic GMP dependent protein kinase 1: implication for neuropathic pain. *Redox Biol*. 2017;11:176-191.
47. Schmidtko A, Luo C, Gao W, Geisslinger G, Kuner R, Tegeder I. Genetic deletion of synapsin II reduces neuropathic pain due to reduced glutamate but increased GABA in the spinal cord dorsal horn. *Pain*. 2008;139:632-643.
48. Tegeder I, Costigan M, Griffin RS, et al. GTP cyclohydrolase and tetrahydrobiopterin regulate pain sensitivity and persistence. *Nat Med*. 2006;12:1269-1277.
49. Fischer C, Endle H, Schumann L, et al. Prevention of age-associated neuronal hyperexcitability with improved learning and attention upon knockout or antagonism of LPAR2. *Cell Mol Life Sci*. 2021;78(3):1029-1050.
50. Brunkhorst-Kanaan N, Klatt-Schreiner K, Hackel J, et al. Targeted lipidomics reveal derangement of ceramides in major depression and bipolar disorder. *Metabolism*. 2019;95:65-76.

51. Luo M, Fee MS, Katz LC. Encoding pheromonal signals in the accessory olfactory bulb of behaving mice. *Science*. 2003;299:1196-1201.
52. Schömel N, Gruber L, Alexopoulos SJ, et al. UGCG overexpression leads to increased glycolysis and increased oxidative phosphorylation of breast cancer cells. *Sci Rep*. 2020;10:8182.
53. Altmann C, Hardt S, Fischer C, et al. Progranulin overexpression in sensory neurons attenuates neuropathic pain in mice: role of autophagy. *Neurobiol Dis*. 2016;96:294-311.
54. Stichel CC, Zhu XR, Bader V, Linnartz B, Schmidt S, Lubbert H. Mono- and double-mutant mouse models of Parkinson's disease display severe mitochondrial damage. *Hum Mol Genet*. 2007;16:2377-2393.
55. Manczak M, Mao P, Calkins MJ, et al. Mitochondria-targeted antioxidants protect against amyloid-beta toxicity in Alzheimer's disease neurons. *J Alzheimers Dis*. 2010;20(Suppl 2):S609-S631.
56. Gaudioso A, Garcia-Rozas P, Casarejos MJ, Pastor O, Rodriguez-Navarro JA. Lipidomic alterations in the mitochondria of aged Parkin null mice relevant to autophagy. *Front Neurosci*. 2019;13:329.
57. Li H, Ham A, Ma TC, et al. Mitochondrial dysfunction and mitophagy defect triggered by heterozygous GBA mutations. *Autophagy*. 2019;15:113-130.
58. Plotegher N, Perocheau D, Ferrazza R, et al. Impaired cellular bioenergetics caused by GBA1 depletion sensitizes neurons to calcium overload. *Cell Death Differ*. 2020;27(5):1588-1603.
59. Wei X, He S, Wang Z, et al. Fibroblast growth factor 1attenuates 6-hydroxydopamine-induced neurotoxicity: an in vitro and in vivo investigation in experimental models of parkinson's disease. *Am J Transl Res*. 2014;6:664-677.
60. de Yebenes JG, Pernaute RS, Garrido JM, et al. Long-term intracerebral infusion of fibroblast growth factors restores motility and enhances F-DOPA uptake in parkinsonian monkeys. *Parkinsonism Relat Disord*. 1998;4:147-158.
61. Oellig C, Pirvola U, Taylor L, Elde R, Hökfelt T, Pettersson RF. Acidic FGF and FGF receptors are specifically expressed in neurons of developing and adult rat dorsal root ganglia. *Eur J Neurosci*. 1995;7:863-874.
62. Mohiuddin L, Fernyhough P, Tomlinson DR. Acidic fibroblast growth factor enhances neurite outgrowth and stimulates expression of GAP-43 and T alpha 1 alpha-tubulin in cultured neurones from adult rat dorsal root ganglia. *Neurosci Lett*. 1996;215:111-114.
63. Glueckert R, Bitsche M, Miller JM, et al. Deafferentation-associated changes in afferent and efferent processes in the guinea pig cochlea and afferent regeneration with chronic intrascalar brain-derived neurotrophic factor and acidic fibroblast growth factor. *J Comp Neurol*. 2008;507:1602-1621.
64. Luo L, Koutnouyan H, Baird A, Ryan AF. Acidic and basic FGF mRNA expression in the adult and developing rat cochlea. *Hear Res*. 1993;69:182-193.
65. Bugra K, Olivier L, Jacquemin E, Laurent M, Courtois Y, Hicks D. Acidic fibroblast growth factor is expressed abundantly by photoreceptors within the developing and mature rat retina. *Eur J Neurosci*. 1994;6:1062.
66. Torres-Odio S, Key J, Hoepken HH, et al. Progression of pathology in PINK1-deficient mouse brain from splicing via ubiquitination, ER stress, and mitophagy changes to neuroinflammation. *J Neuroinflammation*. 2017;14:154.
67. Liss B, Haeckel O, Wildmann J, Miki T, Seino S, Roeper J. K-ATP channels promote the differential degeneration of dopaminergic midbrain neurons. *Nat Neurosci*. 2005;8:1742-1751.
68. Hardie RC. TRP channels and lipids: from Drosophila to mammalian physiology. *J Physiol*. 2007;578:9-24.
69. Prescott ED, Julius D. A modular PIP2 binding site as a determinant of capsaicin receptor sensitivity. *Science*. 2003;300:1284-1288.
70. Qin F. Regulation of TRP ion channels by phosphatidylinositol-4,5-bisphosphate. *Handb Exp Pharmacol*. 2007;509-525. https://doi.org/10.1007/978-3-540-34891-7_30.
71. Brumovsky P, Villar MJ, Hokfelt T. Tyrosine hydroxylase is expressed in a subpopulation of small dorsal root ganglion neurons in the adult mouse. *Exp Neurol*. 2006;200:153-165.
72. Lin CH, Chao CC, Wu SW, et al. Pathophysiology of small-fiber sensory system in parkinson's disease: skin innervation and contact heat evoked potential. *Medicine*. 2016;95:e3058.
73. Numazaki M, Tominaga M. Nociception and TRP channels. *Curr Drug Targets CNS Neurol Disord*. 2004;3:479-485.
74. Tominaga M, Caterina MJ. Thermosensation and pain. *J Neurobiol*. 2004;61:3-12.
75. Brenneis C, Kistner K, Puopolo M, et al. Phenotyping the function of TRPV1-expressing sensory neurons by targeted axonal silencing. *J Neurosci*. 2013;33:315-326.
76. Li L, Rutlin M, Abraira VE, et al. The functional organization of cutaneous low-threshold mechanosensory neurons. *Cell*. 2011;147:1615-1627.
77. Devigili G, Tugnoli V, Penza P, et al. The diagnostic criteria for small fibre neuropathy: from symptoms to neuropathology. *Brain*. 2008;131:1912-1925.
78. Kilpatrick BS, Magalhaes J, Beavan MS, et al. Endoplasmic reticulum and lysosomal Ca(2)(+) stores are remodelled in GBA1-linked Parkinson disease patient fibroblasts. *Cell Calcium*. 2016;59:12-20.
79. Magalhaes J, Gegg ME, Migdalska-Richards A, Doherty MK, Whitfield PD, Schapira AH. Autophagic lysosome reformation dysfunction in glucocerebrosidase deficient cells: relevance to Parkinson disease. *Hum Mol Genet*. 2016;25:3432-3445.
80. Biegstraaten M, Mengel E, Marodi L, et al. Peripheral neuropathy in adult type 1 Gaucher disease: a 2-year prospective observational study. *Brain*. 2010;133:2909-2919.
81. Murugesan V, Chuang WL, Liu J, et al. Glucosylsphingosine is a key Biomarker of Gaucher disease. *Am J Hematol*. 2016;91:1082-1089.
82. Rolfs A, Giese AK, Grittner U, et al. Glucosylsphingosine is a highly sensitive and specific biomarker for primary diagnostic and follow-up monitoring in Gaucher disease in a Non-Jewish, Caucasian cohort of Gaucher disease patients. *PLoS One*. 2013;8:e79732.
83. Strasberg P. Cerebrosides and psychosine disrupt mitochondrial functions. *Biochem Cell Biol*. 1986;64:485-489.
84. Igisu H, Nakamura M. Inhibition of cytochrome c oxidase by psychosine (galactosylsphingosine). *Biochem Biophys Res Commun*. 1986;137:323-327.
85. Hayashida K, Oyanagi S, Mizutani Y, Yokochi M. An early cytoplasmic change before Lewy body maturation: an ultrastructural study of the substantia nigra from an autopsy case of juvenile parkinsonism. *Acta Neuropathol*. 1993;85:445-448.
86. Trimmer PA, Swerdlow RH, Parks JK, et al. Abnormal mitochondrial morphology in sporadic Parkinson's and Alzheimer's disease cybrid cell lines. *Exp Neurol*. 2000;162:37-50.
87. Roy S, Wolman L. Ultrastructural observations in Parkinsonism. *J Pathol*. 1969;99:39-44.
88. Chen Y, Dorn GW 2nd. PINK1-phosphorylated mitofusin 2 is a Parkin receptor for culling damaged mitochondria. *Science*. 2013;340:471-475.
89. Geisler S, Holmstrom KM, Skujat D, et al. PINK1/Parkin-mediated mitophagy is dependent on VDAC1 and p62/SQSTM1. *Nat Cell Biol*. 2010;12:119-131.
90. Kawajiri S, Saiki S, Sato S, et al. PINK1 is recruited to mitochondria with parkin and associates with LC3 in mitophagy. *FEBS Lett*. 2010;584:1073-1079.
91. Zhao Y, Ren J, Padilla-Parra S, Fry EE, Stuart DI. Lysosome sorting of β-glucocerebrosidase by LIMP-2 is targeted by the mannose 6-phosphate receptor. *Nat Commun*. 2014;5:4321.
92. Reczek D, Schwake M, Schröder J, et al. LIMP-2 is a receptor for lysosomal mannose-6-phosphate-independent targeting of beta-glucocerebrosidase. *Cell*. 2007;131:770-783.

93. Tegeder I, Kögel D. When lipid homeostasis runs havoc: lipotoxicity links lysosomal dysfunction to autophagy. *Matrix Biol*. 2020. https://doi.org/10.1016/j.matbio.2020.11.005.
94. Wang W, Zhang X, Gao Q, et al. TRPML1: an ion channel in the lysosome Drosophila TRPML forms PI(3,5)P2-activated cation channels in both endolysosomes and plasma membrane. *Handb Exp Pharmacol*. 2014;222:631-645.
95. Shen D, Wang X, Li X, et al. Lipid storage disorders block lysosomal trafficking by inhibiting a TRP channel and lysosomal calcium release. *Nat Commun*. 2012;3:731.
96. Gómez NM, Lu W, Lim JC, et al. Robust lysosomal calcium signaling through channel TRPML1 is impaired by lysosomal lipid accumulation. *FASEB J*. 2018;32:782-794.
97. Bhave G, Hu H-J, Glauner KS, et al. Protein kinase C phosphorylation sensitizes but does not activate the capsaicin receptor transient receptor potential vanilloid 1 (TRPV1). *Proc Natl Acad Sci USA*. 2003;100(21):12480-12485.
98. Van Buren JJ, Bhat S, Rotello R, Pauza ME, Premkumar LS. Sensitization and translocation of TRPV1 by insulin and IGF-I. *Mol Pain*. 2005;1:17.
99. Susankova K, Tousova K, Vyklicky L, Teisinger J, Vlachova V. Reducing and oxidizing agents sensitize heat-activated vanilloid receptor (TRPV1) current. *Mol Pharmacol*. 2006;70:383-394.
100. Rosenbaum T, Gordon-Shaag A, Munari M, Gordon SE. Ca2+/calmodulin modulates TRPV1 activation by capsaicin. *J Gen Physiol*. 2004;123:53-62.
101. Zhang X, Huang J, McNaughton PA. NGF rapidly increases membrane expression of TRPV1 heat-gated ion channels. *EMBO J*. 2005;24:4211-4223.
102. Yao J, Qin F. Interaction with phosphoinositides confers adaptation onto the TRPV1 pain receptor. *PLoS Biol*. 2009;7:e1000046.
103. Zimmer B, Angioni C, Osthues T, et al. The oxidized linoleic acid metabolite 12,13-DiHOME mediates thermal hyperalgesia during inflammatory pain. *Biochim Biophys Acta*. 2018;1863:669-678.
104. Sisignano M, Angioni C, Park CK, et al. Targeting CYP2J to reduce paclitaxel-induced peripheral neuropathic pain. *Proc Natl Acad Sci USA*. 2016;113(44):12544-12549.
105. Batta G, Soltesz L, Kovacs T, et al. Alterations in the properties of the cell membrane due to glycosphingolipid accumulation in a model of Gaucher disease. *Sci Rep*. 2018;8:157.
106. West AP, Khoury-Hanold W, Staron M, et al. Mitochondrial DNA stress primes the antiviral innate immune response. *Nature*. 2015;520:553-557.
107. Mathur V, Burai R, Vest RT, et al. Activation of the STING-dependent type I interferon response reduces microglial reactivity and neuroinflammation. *Neuron*. 2017;96:1290-302.e6.

SUPPORTING INFORMATION

Additional supporting information may be found online in the Supporting Information section.

Fig S1
Fig S2
Fig S3
Fig S4
Fig S5
Fig S6
Fig S7
Fig S8
Fig S9
Table S1

How to cite this article: Valek L, Tran B, Wilken-Schmitz A, et al. Prodromal sensory neuropathy in *Pink1*$^{-/-}$*SNCA*^{A53T} double mutant Parkinson mice. *Neuropathol Appl Neurobiol*. 2021;47(7):1060–1079. https://doi.org/10.1111/nan.12734